THE ASTROPHYSICAL JOURNAL, 545:454–474, 2000 December 10

MODELING THE VARIABLE CHROMOSPHERE OF α ORIONIS[1]

A. LOBEL[2] AND A. K. DUPREE
Harvard-Smithsonian Center for Astrophysics, 60 Garden Street, Cambridge MA 02138; alobel@cfa.harvard.edu, adupree@cfa.harvard.edu
Received 2000 March 10; accepted 2000 July 27

ABSTRACT

A spectral analysis of the prototypical red supergiant star α Ori that is based on near-UV, optical, and near-IR high-dispersion spectra obtained between 1992 September and 1999 July with the Space Telescope Imaging Spectrograph and the Goddard High Resolution Spectrograph on the *Hubble Space Telescope*, the Utrecht Echelle Spectrograph, and the SoFin Echelle Spectrograph is presented. With detailed non-LTE radiative transfer calculations in spherical geometry, we model the mean conditions in the stellar chromosphere from Hα and the Mg II resonance doublet. The Hα absorption line emerges from an extended chromosphere. Temporal changes of its velocity structure are determined from detailed fits to near-UV Si I lines, and chromospheric expansion velocities around 4 km s^{-1} are found in 1992, whereas the chromosphere was collapsing onto the photosphere with a velocity of 5 km s^{-1} in 1998–1999. The Hα core depth is correlated over time with weaker depression changes seen in prominent TiO band heads that dominate the optical spectrum. From elaborate spectral synthesis calculations, we isolate unblended metal absorption lines in the near-IR and determine $T_{\rm eff} = 3500$ K and $\log(g) = -0.5$ for solar metallicity and 12 ± 0.5 km s^{-1} for macrobroadening and $v \sin i$. Semiempirical fits yield chromospheric temperatures not in excess of 5500 K, but with long-term changes by ~400 K. The model extends over 5000 $R_\odot$ and requires supersonic microturbulence values ranging to 19 km s^{-1}, in strong contrast with the photospheric value of only 2 km s^{-1}. We observe Doppler shifts of 4–8 km s^{-1} in the scattering cores of many double-peaked near-UV emission lines which correlate with changes in the intensity ratio of their emission components. The red emission components were much stronger in 1992, indicating a phase of enhanced chromospheric outflow, for which we determine a spherical mass-loss rate of $6 \times 10^{-7}\ M_\odot$ yr $^{-1}$. We present a discussion of chromospheric pulsation in this massive star. Detailed modeling of the observed Mg II *h* and *k* line asymmetry is also presented. We demonstrate that a chromospheric Mn I blend strongly contributes to this puzzling asymmetry.

Subject headings: line: identification — stars: chromospheres — stars: individual (α Orionis) — stars: late-type — stars: mass loss — supergiants

1. INTRODUCTION

α Orionis (Betelgeuse, HD 39801) is an exceptional star with exceptional spectral properties. Few late-type supergiants (Iab) are or have been studied so intensely over different wavelength regions. This nearby M2 star displays many strong metal emission lines in its ultraviolet (UV) spectrum, which form in a very extended chromosphere. It is a bright target that offers a unique laboratory for understanding the physics of chromospheres in general and its dynamics in particular. Weymann (1962) suggested that the self-reversals in bright emission lines near 3200 Å result from possible absorptions in a cool circumstellar envelope. Based on these lines, some authors have found that material can fall toward the photosphere (Boesgaard & Magnan 1975; Boesgaard 1979), while van der Hucht et al. (1979), Carpenter (1984), and Carpenter & Robinson (1997) found from space-borne near-UV data indications of circumstellar outflow. Like many studies of optical data that point to photospheric pulsations (Dupree et al. 1987; Smith, Patten, & Goldberg 1989), these UV observations also hint to pulsations of α Ori's chromosphere. However, studies that focus on modeling chromospheric inflow and outflow for supergiants have not been carried out to date because of the lack of high-quality spectra in this wavelength region, which also cover a sufficiently long period of time.

For this paper, a set of *HST* spectra observed between 1992 and 1999 has been collected and combined to allow a detailed modeling of α Ori's chromospheric dynamics. We combine a sequence of high-resolution spectra taken in the near-UV with the Space Telescope Imaging Spectrograph (STIS) with spectra from the Goddard High Resolution Spectrograph (GHRS), together with ground-based high-dispersion optical and near-IR spectra. This unique combination enables modeling of the stellar photosphere, in conjunction with the variable chromospheric conditions, based on detailed fits to selected line profiles formed over these different atmospheric regions.

This is the first time a self-consistent semiempirical spectral modeling of Betelgeuse's extended atmosphere that considers radiative transfer in spherical geometry and a detailed spectral synthesis to check and account for line blending in this cool star has been made. Atomic and molecular opacity sources are combined in our spectral fits, and constraints on various line-broadening mechanisms are incorporated to infer atmospheric and dynamic conditions.

The paper is organized as follows. Section 2 contains a brief description of all the data, the individual reduction procedures, and their corresponding calibration accuracies. Section 3 gives semiempirical constraints from optical spectra to the conditions in the stellar photosphere and presents a discussion of variations observed in prominent molecular bands. In § 4, this photospheric model is applied

[1] Based in part on observations with the NASA/ESA *Hubble Space Telescope* obtained at the Space Telescope Science Institute, which is operated by AURA, Inc., under NASA contract NAS 5-26555.

[2] Guest investigator of the UK Astronomy Data Centre.

to constrain the chromospheric parameters from elaborate radiative transfer fits to selected near-UV emission-line profiles. This model is used in § 5 to determine its detailed velocity structure during phases of inflow. In § 6, we model phases of outflow and discuss the properties of these dynamics over time.

2. OBSERVATIONS AND DATA REDUCTION

2.1. *HST Near-Ultraviolet Spectra*

Observations of α Ori were obtained with the smallest aperture available to the STIS. The field of view of 25 mas by 100 mas covers less than one quarter of the UV disk area. The mean UV disk diameter derived from Faint Object Camera (FOC) imaging in 1995 is about 120 mas (Gilliland & Dupree 1996). These echelle spectra were obtained for three offset pointings of 25 mas by scanning left and right in the cross-dispersion direction from the central intensity peakup. The pointing positions for the spectral scan of 1998 September are shown in Figure 1 and marked by the crosses. The mean pointing jitter in the *HST* fine-clock mode remained below 3.5 mas, which is typical for all other raster scans. Our spectra are hence truly spatially resolved, unlike the GHRS spectral scan of 1995 March, where a square field of view of 200 mas was utilized (Uitenbroek, Dupree, & Gilliland 1998). Table 1 summarizes the STIS observations of our HST proposal No. 7347, but it also includes another near-UV GHRS spectrum obtained from the *HST* Data Archive, which is studied in this paper. Four STIS raster scans were taken with the E230M grating, providing $R \sim 30{,}000$ in the spectral range between 2275 and 3120 Å. The single-exposure times range from 280 s at the central scan positions to 550 s near the stellar limb, providing signal-to-noise ratios (S/N) between 25 and 40 for global count rates up to 3000 s^{-1}. The scan axes in the plane of the sky across the UV disk were almost parallel (within 10°) to the east-west direction, except for 1998 January, when the scan axis was tilted by −40°.

The observations of 1998 April were complemented by an additional spectral scan utilizing the E230H grating, which provided very high resolution ($R \sim 114{,}000$) near-UV spectra. Here the projected slit area was increased to 63 mas by 200 mas, and the aperture center was placed at pointing offsets of 63 mas and 126 mas (left and right of intensity peakup). Hence, the UV limb was exposed out to 157.5 mas. For similar exposure times as with E230M, the higher throughput of this bigger slit provided useful spectra just off the UV disk edge. But because of the higher spectral resolution, the five spectra cover a smaller spectral range between 2666 and 2942 Å. These spectra are also useful in this study in terms of measuring the degrading effect of the medium-resolution E230M grating on the detailed shape of weak near-UV emission lines (e.g., the intensity ratios of their double-peaked cores). In most cases, the effect of the

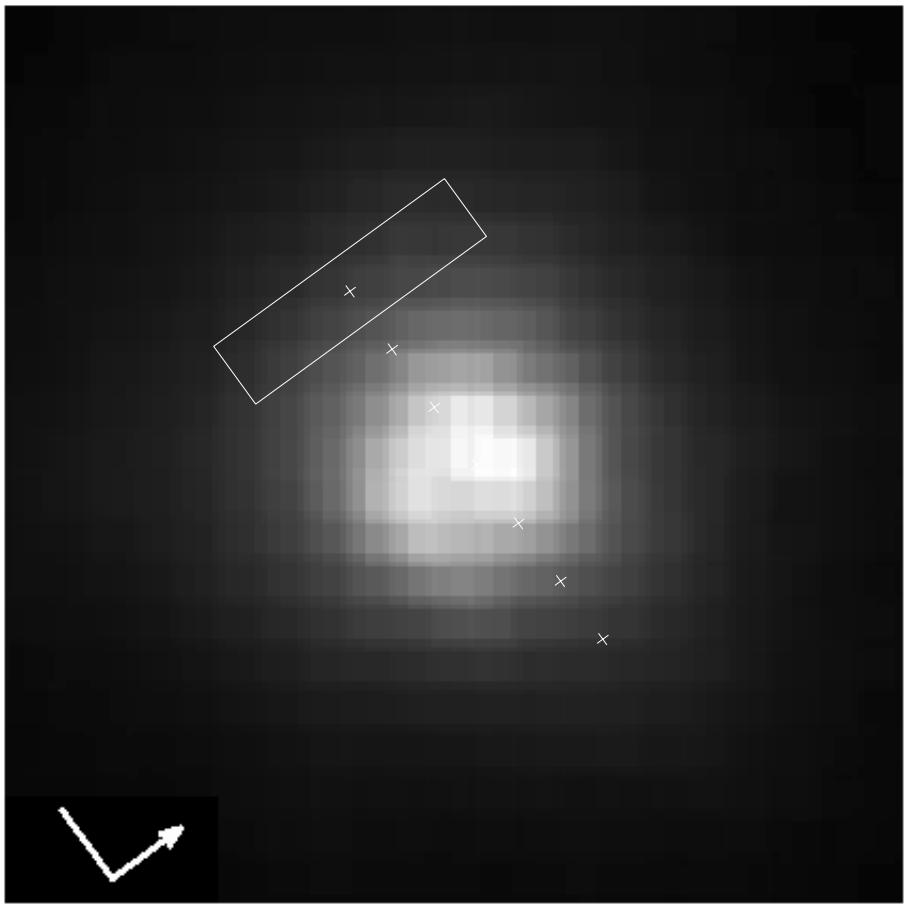

FIG. 1.—Four *HST* Faint Object Camera images (with 1 pixel = 14.35 mas) of α Ori on 1998 September 14 are coaligned into a sum image that reveals an "arclike" brightness structure spanning a large portion of the UV disk. The slit positions of the spatially resolved spectral raster scan with the STIS are shown for the 100 by 25 mas aperture. The arrow points to the north in the plane of the sky (east is left).

TABLE 1

NEAR-ULTRAVIOLET, OPTICAL, AND NEAR-INFRARED SPECTRA OF α ORI USED IN THIS ANALYSIS

Telescope-Instrument	Observation Date	Start Time (UT)	Wavelength Range (Å)	Grating Name	Aperture (mas)	R	Number of Exposures	Exposure Time (s)
Whipple Obs.	1985 Sep 25	11:28	3913–3949	Echelle	[b]	36,600	1	2700
HST-GHRS	1992 Sep 24	12:21	2791–2806	ECH-B	200 × 200	85,000	1	1292
HST-GHRS	1992 Sep 24	03:12	1980–3300	G270M	200 × 200	~30,000	33[a]	700
WHT-UES	1993 Jan 13	22:26	5000–9000	E31(42)	[b]	52,000	1	100
WHT-UES	1993 Feb 12	20:05	5000–9000	E79(18)	[b]	49,000	4	0.5
WHT-UES	1993 Feb 12	20:23	5000–9000	E79(18)	[b]	49,000	4[c]	0.5
WHT-UES	1996 May 1	20:29	5000–9000	E79(18)	[b]	49,000	4	1
HST-STIS	1998 Jan 8	09:30	2275–3130	E230M	100 × 25	30,000	7[d]	280–550
HST-STIS	1998 Apr 1	14:47	2275–3130	E230M	100 × 25	30,000	7[d]	280–550
HST-STIS	1998 Apr 1	17:34	2666–2942	E230H	200 × 63	114,000	5[d]	280–550
HST-STIS	1998 Sep 24	03:08	2275–3130	E230M	100 × 25	30,000	7[d]	280–550
HST-STIS	1999 Mar 28	06:07	2275–3130	E230M	100 × 25	30,000	7[d]	280–550
NOT-SoFin	1998 Oct 11	05:35	2000–12000	Cam3	[b]	~30,000	5	20
NOT-SoFin	1999 Jul 31	06:32	10000–11000	Cam1	[b]	160,000	1	40

[a] Single-exposures over different wavelength regions of 43 Å wide.
[b] Projected slit width integrates optical and near-IR disk. Separate exposures are coadded.
[c] Central wavelength setting increased by 40 Å to cover echelle gaps.
[d] STIS spatially resolved single-exposure spectra in raster scan across UV disk for variable exposure times.

instrumental broadening proved to be unimportant, owing to their large intrinsic broadening (see § 6). For an extended UV source such as α Ori, the FWHM of the echelle line spread function for the NUV-MAMA detectors with the medium- and high-resolution gratings (and the above-mentioned apertures) are ~1 and ~2 pixels, respectively. Weak emission lines observed with medium resolution display FWHM values exceeding 14 pixels, where 1 pixel ≃ 5 km s^{-1}. After converting to air wavelengths, we measure for the high-resolution spectra that 1 pixel ≃ 1.3 km s^{-1}.

The disk-integrated GHRS spectra in Table 1 were observed on 1992 September 24. They have been published and discussed in Brandt et al. (1995) and Robinson & Carpenter (1995). High-resolution GHRS spectra of the Mg II resonance doublet were observed with $R \sim 85{,}000$. The good S/N of ~30 and calibration accuracy of 0.3 km s^{-1} allows a comparison with the high-resolution STIS spectra. Another series of medium-resolution GHRS spectra were also obtained with $R \sim 20{,}000$–$35{,}000$, covering 1980 to 3300 Å, with a wavelength calibration accuracy of 2 km s^{-1}. For our comparisons, we have retrieved these calibrated spectra through the *HST* Data Archive.

All of the STIS spectra were (re)calibrated using the CALSTIS 2.0 software package under IRAF-STSDAS. The individual steps of the full STIS reduction pipeline can be consulted in chapters 19–23 of the *Hubble Space Telescope Data Handbook*.[3] Most important is that our recalibrations were performed with the most recently updated calibration reference files (flat fields, aperture throughput tables, etc.), which we have installed in the pipeline. The wavelength calibration (which also includes corrections for orbital spacecraft motion) is limited by thermal drifts, deviations in determining the zero-point calibration position of the exposures, possible optical distortions, and corrections for small-scale geometric distortion of the MAMA detectors. The accuracy of the dispersion solutions in absolute wavelengths is typically between 0.5 and 1.0 pixels, corresponding to the above given accuracies in km s^{-1}.

The accuracy of the line-flux calibrations are limited by scattered light from the echelle, *HST*'s Optical Telescope Assembly (the truss structure supporting the primary and secondary mirrors) point-spread function and the detector, into the interorder areas. This may result in an oversubtraction of the background and thus affect the resulting line depressions. However, current STIS performance monitoring indicates that the E230M and E230H gratings are affected only by scattered light to 4% at 2500 Å (see *STIS Instrument Handbook*, chap. 13)[4], which is comparable to the S/N of our spectra. The flux calibrations are further limited by ripple corrections and nonuniformity of flat fields with the stability of the instrument (which amounts to ~5%). STIS-MAMA flats have shown evidence for variation at the 1%–2% level per resolution element over roughly year timescales. These changes remain limited, allowing emission-line intensities in these spectra obtained between 1998 January and 1999 March to be compared. However, the principal focus here is the detection of changes in observed line shapes and widths.

2.2. *Optical and Near-Infrared Spectra*

Optical echelle spectra of α Ori have been obtained on 1993 January 13, 1993 February 12, and 1996 May 1 in the range between 5000 and 9000 Å with the Utrecht Echelle Spectrograph (UES) at the Nasmyth focus of the 4.2 m William Herschel Telescope at the Observatorio del Roque de los Muchachos (La Palma). These spectra were retrieved from the UES Archive (UK Astronomy Data Center) and reduced by us with the standard IRAF procedures. The wavelength calibration was performed with a Th-Ar lamp, and the dispersion solutions are iterated to accuracies typically better than 0.02 Å. The three spectra have $R \sim 50{,}000$, but only the spectrum of 1993 January covers this entire spectral range over 42 echelle orders. The spectra of 1996 and of 1993 February cover only 18 orders. However, the latter observations consist of four subsequent exposures repeated for two central wavelength settings by 40 Å apart. The reduced sum spectra provide an S/N that varies over the echelle orders in the range of 50 to 100. These spectra were observed in conditions with weak telluric absorption, but the spectrum of 1993 January has been exposed through a cloud for 100 s, thus producing saturated water vapor bands in certain spectral regions.

The STIS spectra of 1998 September were complemented by an optical spectrum of α Ori obtained on 1998 October 11 with the SoFin Echelle Spectrograph (Nordic Optical Telescope, La Palma). It covers the range between 3600 Å and 1.2 μm with $R \sim 30{,}000$. A separate exposure was obtained in the near-IR in search of He I 10830 Å. This line was not detected, but thorough spectral synthesis modeling revealed a number of unblended metal absorption lines in this region. Surprisingly, this spectral region in an M-type star appears practically free of molecular absorption bands. The three isolated Ni I, Cr I, and Fe I lines display fluxes in the wings within 5% of the stellar continuum level (see § 3). These lines therefore were observed again on 1999 July 31 using the high-resolution camera ($R \sim 160{,}000$) with S/N ~ 50, and kindly provided by I. Ilyin (1999, private communication). The optical spectra are wavelength calibrated by Th-Ar comparison spectra, but the near-IR calibration also invokes sharp telluric lines. Reductions were done with the 3A software package (Ilyin 1997),[5] which includes removal of scattered light and the blaze correction. Unlike the STIS spectra, neither the UES nor the SoFin spectra have been calibrated in the absolute flux scale, and their normalizations to the continuum level are accomplished via elaborate spectral synthesis calculations (R. Kurucz, 1999, private communication).

3. PHOTOSPHERIC MODEL PARAMETERS

The many strong emission lines observed in the near-UV spectra of Betelgeuse emerge from a warmer envelope around the stellar photosphere. In § 4, we will semi-empirically constrain the mean model parameters such as kinetic temperature, density, and velocity profile of this chromosphere from detailed fits to selected spectral lines. To reach this goal, good knowledge of the circumstances in the deeper atmospheric layers is required to develop an extended atmospheric model by means of detailed radiative transfer calculations. α Ori is known to pulsate in quasi-

[3] The STScI, 1999, *Hubble Space Telescope Data Handbook*, Version 3.1, is available at http://www.stsci.edu/documents/data-handbook.html.

[4] The STScI, 1999, *STIS Instrument Handbook*, Version 3.0 is available at http://www.stsci.edu/cgi-bin/stis?cat=documents&subcal=ihb.

[5] I. Ilyin's 1997 *Acquisition, Archiving, and Analysis* (*3A*) *Software Package User*'s Manual is available at http://www.not.iac.es/newwww/html/sofin.html.

periods of ~420 days, as observed from the visual light curve and from radial velocity measurements (Dupree et al. 1987; Smith et al. 1989). Such pulsation might be accompanied by photospheric temperature changes. For example, Morgan, Wasatonic, & Guinan (1997) discussed changes of $T_{\rm eff}$ from ~3550 to ~3450 K, observed between 1996 September and 1997 April, which they infer from narrowband photometry in Wing's three-color filter system (Wing 1992). One passband measures absorption changes in the TiO band head at 7190 Å that are associated with variations of the atmospheric temperature, presumably caused by pulsation. Di Benedetto (1993) suggests 3620 ± 90 K from other photometric comparisons. But $T_{\rm eff}$ determinations derived from angular diameter measurements range from 3190 (Bester et al. 1996) to 3605 K (Dyck et al. 1996), whereas older $T_{\rm eff}$ determinations suggest slightly higher values of 3900 ± 150 (Tsuji 1976) and 3800 ± 100 K (Kodaira et al. 1979).

These photospheric model parameters can be tested with the near-IR spectrum of 1999 July. Three unblended absorption metal lines of Ni I λ10302, Cr I λ10801, and Fe I λ10818 can be isolated using extended Kurucz line lists, which also include isotopic and hyperfine splitting lines for the atomic species. With multi-Gaussian fits, the integrated equivalent widths are 89 ± 7 mÅ, 153 ± 9 mÅ (but with a weak OH blend of 21 ± 6 mÅ), and 149 ± 13 mÅ, respectively, for lower excitation energy levels of 4.26, 5.66, and 3.95 eV. Error bars result from placing the normalized continuum level 1% higher and lower. The input line lists from Kurucz also include diatomic molecules such as OH, TiO, CN, and C_2, which are important opacity contributors in this spectral region. Best fits in Figure 2 are derived in LTE

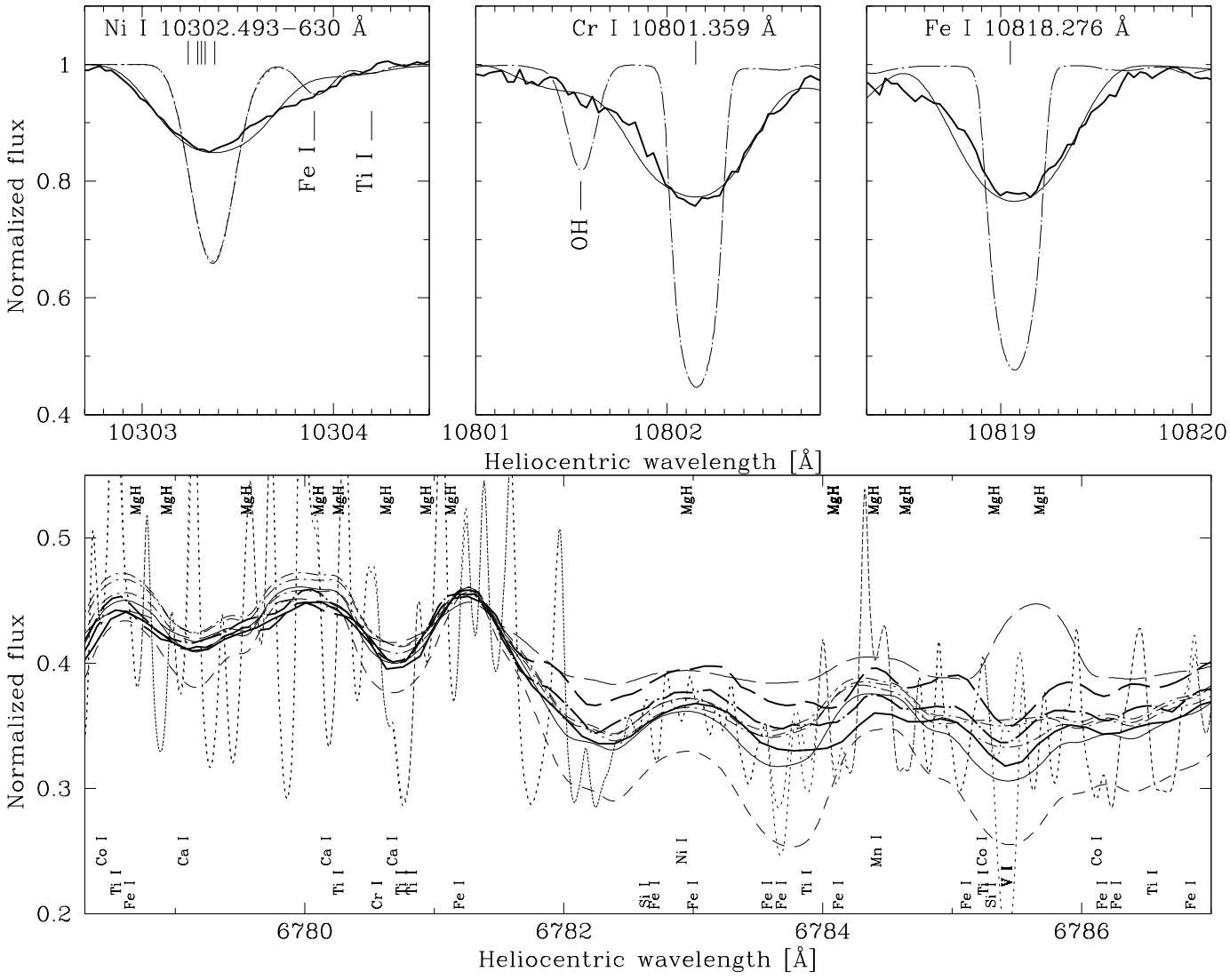

FIG. 2.—*Upper panels:* Photospheric model parameters are derived from a best fit (*thin solid lines*) to profiles of unblended metal absorption lines in the near-IR (*bold solid lines*). Unbroadened synthetic profiles computed with the selected model are shown by the thin dash-dotted lines. Note the isotopic splitting of the Ni I line. *Lower panel:* The depression of the TiO 6781 Å band head in 1998 October (*bold solid line*) is best fit for $T_{\rm eff}$ = 3500 K (*thin solid line*). The synthesized spectrum becomes too strong for 3600 K (*thin short-dashed line*) but saturates below 3300 K (*thin dash-dotted lines*). The band was weaker in 1993 February (*bold dash-dotted line*) and 1996 May (*bold dashed line*). The latter observation can be matched when incorporating a chromosphere (*thin long-dashed line*). The Hα core depth correlates with these contrast changes in TiO bands. The unbroadened synthetic spectrum is shown when computed with and without atomic lines (*thin dotted lines*) (i.e., the contribution of a strong Fe I line near 6783.8 Å can be seen by comparing both). Strong TiO, CN, C_2, and OH lines are not labeled.

for $T_{\rm eff} = 3500 \pm 100$ K, log $(g) = -0.5$, and a projected microturbulence velocity of 2 ± 1 km s^{-1}. Model parameters are derived for solar metallicity (Anders & Grevesse 1989) since an abundance determination would require unblended lines of the same species covering a broad range of excitation energies to remove the effect of formation depth dependency in this extended atmosphere. These LTE calculations are performed with the SYNTHE code in plane-parallel geometry for static and plane-parallel photospheric models from ATLAS12 (Kurucz 1996; Kurucz 1997). The log (gf)-values for the three lines have been normalized to the solar spectrum.[6] We also find that their relative intensities could be slightly better fit for the model with log $(g) = -0.5$ instead of 0.0.

After degrading the synthetic profiles with the instrumental resolution, we obtain best fits for a geometric mean (or the square root of summed squares) of Gaussian macrobroadening and $v \sin i$ of 12 ± 0.5 km s^{-1}. Gray (2000) estimated 11 km s^{-1} from optical spectra of 1996–1998 with comparable resolution. Such large macrobroadening values are not uncommon among supergiants of even higher $T_{\rm eff}$ and smaller photospheric radii than α Ori (i.e., for ρ Cas, see Lobel et al. 1998). For our selected photospheric model, we compute that the adiabatic sound speed ($v_{\rm ad}^2 = \Gamma_1 P/\rho$; with the adiabatic compression modulus $\Gamma_1 \simeq 5/3$ in neutral atomic gas) at the mean formation depth ($\tau_{\rm Ross} \sim 1$) of these lines as 7.6 km s^{-1}. For an expected $v \sin i$ value below 5 km s^{-1}, for this luminous and evolved supergiant (e.g., Pasquini, Brocato, & Pallavicini 1990), the total line broadening of 12 km s^{-1} implies supersonic values for the large-scale convective flow velocity in the stellar photosphere. It is interesting that preliminary three-dimensional numerical simulations of surface convection in supergiants can produce maximum velocities above 6 km s^{-1} (Freytag 2000). Although these models (with 31 cube mesh) are "fully convective" and the core still remains unresolved, giant convection cells *do* form in these simulations, as was proposed by Schwarzschild (1975). In this context, it is also worth noting that other time-dependent three-dimensional hydrodynamic simulations of a complete pulsating red giant star by Jacobs, Porter, & Woodward (1999) (with 512 cube mesh, but without handling important compressibility effects of the partial ionization zones of H and He) show a global surface convection pattern covering the entire star with strong dipolar flow around the core. They also note that the simulated oscillations could be induced by these large-scale convective motions.

Further testing of the selected photospheric parameters is possible from fits to intense TiO bands that dominate the optical spectra of α Ori. In M-type stars, this intense molecular background complicates a modeling based on fits to (unblended) atomic absorption cores because it deeply suppresses their line wings to below the stellar continuum level. For the spectral synthesis, TiO line lists were compiled from the semiempirical data given in Schwenke (1998). These lists typically contain about 1000 lines per angstrom and are computed for the four Ti-isotopes with Earth abundance ratios. We solve the chemical equilibrium by iterating over the (LTE) abundance equations for the molecular and atomic species. For instance, because of this TiO background, the computed spectral energy distribution (SED) of α Ori shows that the local mean level for the Ti I λ6273 absorption line is lowered to ∼0.4 of the normalized stellar continuum level. Note that Gray (2000) normalized the wings of this line to unity in a study of short-term variations observed in optical absorption cores. This causes an overestimate of their depth variations. The entire SED has been computed between 0.2 and 5 μm with high resolution in LTE for our photospheric parameters. This SED table and images are available from the Kurucz website.

In the lower panel of Figure 2, the best fit is shown (*thin solid line*) to the TiO band head observed at 6781 Å in 1998 October. Computations suggest that this band is unblended by atomic lines, which might affect its proper intensity. Absorption in the band head becomes too strong for our model with $T_{\rm eff} = 3600$ K (*thin dashed line*), whereas it is too weak when $T_{\rm eff} = 3400$, 3300, and 3200 K (*thin dash-dotted lines*). At these low temperatures, the contrast of this band with respect to the overall background is reduced as the molecular background (from other TiO lines) strengthens; and the reverse is true for models of higher $T_{\rm eff}$. Interestingly, the strength of this band varies with time. It is 2% weaker in 1993 February (*bold dash-dotted line*) and ∼5% weaker in 1996 May (*bold long-dashed line*) than in 1998 October. Note that the spectra are scaled to the intensity maximum at ∼6781 Å to compare the band depressions over time. Such large depth variations are caused by the temperature sensitivity of TiO in M-type stars earlier than M7 ($T_{\rm eff} \geq 3000$ K) (i.e., Fluks et al. 1994).

The visible magnitude of α Ori passed through a brightness minimum of $V \sim 0\overset{\rm m}{.}9$ in 1993 February (Bester et al. 1996), whereas the star was brighter by $\sim 0\overset{\rm m}{.}3$ in 1996 May (Dupree, Lobel, & Gilliland 1999). These intensity changes in the TiO band heads therefore could be interpreted to result solely from changes in the optical continuum flux caused by temperature changes in the stellar photosphere (i.e., Morgan, Wasatonic, & Guinan 1997). We find, however, strong indications that such an interpretation is flawed. This follows from our observations that there is a strong correlation between the TiO band strength and the depth of the Hα line core. The next section will demonstrate that Hα (with $\chi_{\rm low} \sim 10.15$ eV) cannot be excited sufficiently by a pure photospheric model with $T_{\rm eff} = 3500$ K to match its observed line strength. The computed core depression would remain invisible behind the TiO background, and this photospheric model must therefore be extended with a model of the stellar chromosphere to populate this transition adequately. The LTE radiative transfer calculations demonstrate that the TiO band heads form on average at optical depths higher than $\tau_{\rm Ross} = 10^{-3}$. The observed correlation with Hα therefore strongly suggests related dynamical properties of the photospheric conditions (or lower chromosphere) and the chromospheric variability mechanism.

This important temperature effect of the chromosphere at the mean formation depth of TiO is better seen in Figure 3 from the δ(0–0) band head at 8860 Å. In α Ori, this band has a sharper contrast (with a central normalized flux of ∼0.6) because it is much closer to the stellar continuum level than the band at 6781 Å. The two spectra were observed by only about one month apart (*bold lines*), but we could not detect any significant line-depth changes in the spectra. The synthetic spectrum computed with the selected model is shown by the thin solid line. It matches the depth of the two Fe I

[6] R. L. Kurucz's 1998 document from the 6th Atomic Spectroscopy and Oscillator Strengths Meeting in Victoria (August 1998) is available at http://cfaku5.harvard.edu/linelists/gfall.

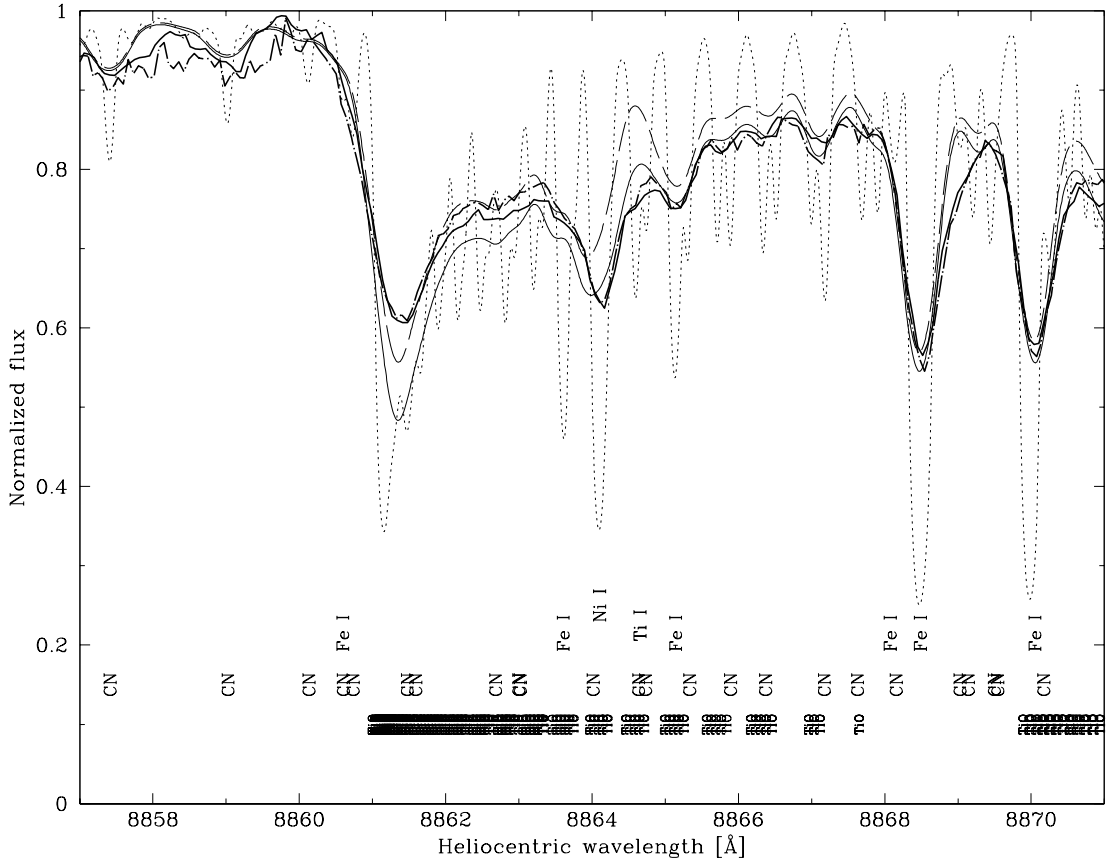

FIG. 3.—The R δ(0–0) TiO band head near 8860 Å observed in α Ori on 1993 January 13 (*bold dash-dotted line*) and February 12 (*bold solid line*) with UES. The synthetic spectrum for the photospheric model with $T_{\rm eff} = 3500$ K is shown by the thin solid line. The computed band head is $\sim$10% too deep, although the cores of the strong Fe I lines do match. By incorporating the chromosphere in the model, the fit to the band head improves without significant changes to the Fe I cores. It demonstrates the different mean formation depth for the band head and for these atomic lines. The unbroadened synthetic spectrum is shown by the dotted line. Intense molecular and atomic lines are labeled.

cores to the right and strongly reproduces the intensity across this entire TiO band. But for this selected model, the computed strength of the band head is clearly too deep by $\sim$10%. We could remove this discrepancy, however, by attaching a model of the chromosphere, as shown in § 4. This modeling also reveals how the chromosphere does not affect the strength of the two Fe I lines since they are formed at much higher optical depths deep in the photosphere. After invoking the chromospheric model, some minor changes in their central intensity result only from small intensity differences in the computed molecular background. Further tests show that this is also the case for the three unblended metal lines in the near-IR, which constrain the photospheric model parameters. We are therefore confident that our $T_{\rm eff} = 3500$ K and log $(g) = -0.5$ are not biased by temperature effects from the chromosphere of α Ori. Carr, Sellgren, & Balachandran (2000) derive $T_{\rm eff} = 3540 \pm 260$ K with a microturbulence of 3.23 ± 0.15 km s^{-1}, for an adopted log $(g) = 0.0$, by modeling equivalent-width values of CO and Fe I lines in high-resolution KPNO Fourier transform spectrograph spectra in the K band, observed in 1980 by Wallace & Hinkle (1996). From a study of 11 Fe I lines, they derive an abundance value equivalent to the solar abundance, which we have adopted here to fit the three near-IR metal lines. Since these authors derive the stellar parameters with photospheric models that do incorporate sphericity effects, it indicates that for lines formed in the deeper photosphere, possible curvature effects remain small since our parameters are almost identical but computed for plane-parallel geometry. However, future studies to detect and estimate possible changes in these photospheric parameters caused by the observed stellar variability should consider effects of the atmospheric curvature in the radiative transfer calculations. A more detailed study of these model parameters is planned with high-resolution synthesis calculations using the PHOENIX code (e.g., see the M-S-C giant model grid released by Allard & Hauschildt 1995), which incorporates spherical geometry. Of current interest is the abundance of lithium in cool stars, but none of our optical spectra showed a detectable signal of the Li I λ6707 resonance doublet against the molecular background.

In summary, the analysis of Betelgeuse's photosphere provides evidence that the strengths of optical TiO band heads are affected by (temperature effects from) the stellar chromosphere. Intensity changes in the band head at 6781 Å correlate in time with the variable Hα core depth, which emerges from this chromosphere. For instance, the weakness of this band observed in 1996 is well matched by incorporating a chromospheric model, which is shown by the thin long-dashed line in Figure 2. These molecular radiative transfer calculations are performed in LTE, thereby sometimes producing unobserved emission lines in the optical. But this effect of the chromosphere, at the mean TiO formation depth in the upper photosphere, is far more important than possible NLTE effects or effects of geomet-

ric curvature at these depths. Note, for instance, that Hauschildt et al. (1997) investigated departures from LTE in giant models with low log (g)-values but found only modest NLTE effects in the abundance of TiO. Our observations for α Ori therefore suggest that caution is needed when calibrating spectral subtypes of M-type giants (or model effective temperatures) based on this TiO R band head depression at 8860 Å (i.e., Plez 1998). Besides improving the molecular line data to achieve an up-to-date accuracy in such relations, one ought also to account for effects from the chromosphere for the individual calibration stars. For α Ori, this temperature effect can amount to ∼10% in the depression of this band. On the other hand, we note that our equation of state currently omits possible effects of TiO^+, and other Ti-bearing molecules on the abundance of TiO. Also, the applied molecular line data for our high-resolution synthesis calculations can be considered as incomplete because mixing between the different TiO band systems has not (yet) been treated in detail.

Recent interferometric imaging of Betelgeuse by Young et al. (2000) in 1997 October/November reveals strong variations in the apparent symmetry of the stellar brightness distribution at 7000, 9050, and 12900 Å. They suggest that the stronger asymmetry seen at shorter wavelengths result from features with higher contrast on the stellar disk because of strong opacity sources (therefore providing a stronger sensitivity to localized temperature changes, i.e., caused by convection plumes) in an extended line-blanketed atmosphere. This appears to be consistent with the intense TiO opacity that dominates the optical SED but which strongly reduces toward the near-IR wavelengths. The local mean flux level of the computed SED between 12000 and 14000 Å approaches the stellar continuum level within a few percent. This absence of strong molecular opacity can explain the featureless center-to-limb brightness profiles observed in these wavelengths.

4. CHROMOSPHERIC MODEL PARAMETERS

4.1. Hα

The conditions of α Ori's chromosphere are constrained from detailed fits to the Hα line core in the UES spectra. The SMULTI code adapted by Harper (1994) is applied. It performs NLTE radiative transfer calculations for multilevel single-atom models in moving media. This code properly invokes the effects of curved atmospheric geometry on emergent spectral line shapes that form in an extended and dynamic chromosphere like that of Betelgeuse. We adopt a hydrogen-model atom that considers nine energy levels (plus the continuum) and 36 line transitions over the different series (the nine continua are treated separately). The population densities are converged using the local operator formalism for a wide range of chromospheric temperature and electron-density structures attached to our photospheric model. The number of iterations, before convergence is achieved, ranges typically up to 30 and is sensitive to the smoothness of the conditions with height in the chromosphere. These semiempirical fits consider a total of 25–30 chromospheric layers at optical depths $\tau_{\rm Ross} \leq 10^{-3}$ (above the mean formation depth of the TiO band heads) and ∼40 layers for the deeper photosphere.

In the lower panel of Figure 4, the photospheric radius R_* is taken as 700 $R_\odot$ at $\tau_{5000} = 1$ (Uitenbroek, Dupree, & Gilliland 1998). We compute line profiles for five light rays intersecting this photospheric core. The upper panel shows the changes over time in the observed (normalized) Hα core depth (*bold lines*). If the radiative transport is evaluated without a chromosphere, the Hα line core submerges in the molecular (and atomic) absorption background. Its normalized core depth does not exceed 0.2 and the line remains invisible (*thin dotted line*). An attached chromospheric temperature- and electron-density structure can sufficiently excite this transition to match its depth of 1996 (with respect to the background) for a temperature minimum of 2700 K (at $\tau_{\rm Ross} \simeq 10^{-3}$) and a maximum of 5050 K, where $N_e = 1\text{–}7 \times 10^7$ cm^{-3} (*thin long-dashed lines*). We find that the chromospheric model must extend at least out to 5000 $R_\odot$ (7.1 R_*), where the contribution function to the Hα line core peaks. The latter value reinforces our current requirement to account for sphericity effects. Note that this "Hα chromospheric radius" of ∼7 R_* extends almost three times farther out than the "UV radius" of 1750 $R_\odot$ assumed in Uitenbroek et al. (1998). The normalized Hα line core was deeper by 0.15 in 1993 (*bold dash-dotted line*), which we model with an increase by ∼400 K and slightly higher N_e values (*thin dash-dotted lines*). The model requires a partial hydrogen ionization fraction ranging to 35% between $3.0 \leq \log (r/R_\odot) \leq 3.5$, which peaks around the temperature maximum. The semiempirical models shown in the lower panel of Figure 4 are listed for both dates in columns (2)–(7) of Table 2 at 71 height points above the stellar radius. The increased chromospheric temperature, which matches the deeper Hα core of 1993, is consistent with the stronger TiO λ6781 band head (see Fig. 2). In this phase, the higher chromospheric temperature weakens its overall molecular background, which produces a better contrast for this band head. Such changes in chromospheric temperature could perhaps result from similar changes of $T_{\rm eff}$ over time, but the (LTE) fits to this band head indicate that an increase by 400 K in $T_{\rm eff}$ would produce contrast changes that are far larger than observed.

Our modeling also requires high microturbulence values in the chromosphere to match the observed Hα core width, shown in the bottom panel of Figure 4. These values range to 19 km s^{-1}, in stark contrast with only 2 ± 1 km s^{-1} indicated by the photospheric metal lines. Note that the wave-driven models of Hartmann & Avrett (1984) result in chromospheric microturbulence values to 11 km s^{-1}, or about a factor of 2 smaller than our semiempirical models. These highly supersonic microturbulence values mask the detection of small radial-velocity variations in this broad line core. The *Hipparcos* (ESA 1997)[7] stellar transverse velocity is drawn at +18.27 km s^{-1} (*vertical dotted line in upper panel* of Fig. 4). The actual Hα core profile is correctly fit for a macrobroadening and $v \sin i$ of 18 ± 1 km s^{-1}. This value is obtained after degrading the computed line profile (multiplied with its normalized molecular background) with the instrumental profile. The Hα line core is clearly distorted and appears asymmetric because of a hyperfine splitting band of Co I lines (Kurucz 1993) in its red wing. Similar fits to the Hβ core (with a normalized depth ∼5% deeper than Hα) of 1998 October also provide 18 ± 1 km s^{-1}. But the overall fit to this line profile is not as satisfactory because of the lack of the VO band at 4858.7 Å (of the Yellow-Green system, see Harrington et al. 1970) in our background opacities. We could not detect Balmer lines

[7] See also http://astro.estec.esa.nl/Hipparcos/table365-new.html.

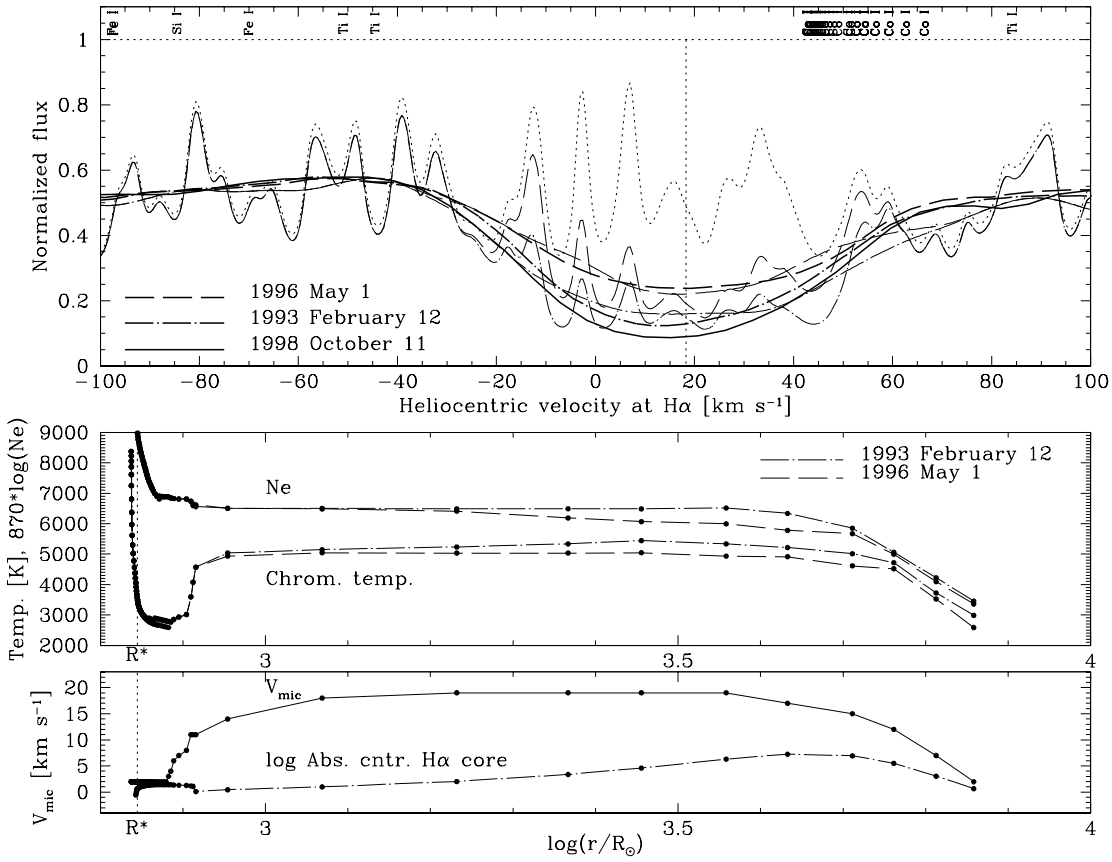

FIG. 4.—*Upper panel:* Three Hα profiles observed in 1998 October (*bold solid line*), 1996 May (*bold dashed line*), and 1993 February (*bold dash-dotted line*) indicate long-term variations in the conditions of α Ori's chromosphere. The unbroadened synthetic spectrum computed without a chromosphere is shown by the dotted line. With the model of the chromosphere, Hα becomes sufficiently excited and fits the core profile of 1993 and 1996 (*thin broken lines*) for the temperature and electron density structures shown in the lower panel. With this instrumental resolution, the fit to this broad core requires a macro-broadening and $v \sin i$ of 18 km s^{-1}. The normalized continuum level and centers of strong atomic lines are marked. Note also the hyperfine splitting band of Co I in the red wing. *Lower panels:* The temperature structure of the outer chromosphere changes by ~400 K between 1993 and 1996 with highly supersonic microturbulence values that produce the profiles in the upper panel. For comparison, the absorption contribution function for the Hα core is shown on a logarithmic intensity scale in the lowest panel, peaking around 5000 $R_\odot$ (7.1 R_* for $R_* = 700\,R_\odot$ at $\tau_{5000} = 1$).

other than Hα and Hβ against the molecular and atomic background in the spectra.

This value of 18 km s^{-1} differs significantly from the broadening velocity of only 12 km s^{-1} derived from fits to the photospheric metal lines. Jennings & Sada (1998) also measure a broadening of 12 km s^{-1} from rotational water vapor absorption lines detected in the mid-IR. They compute an upper limit for the temperature in the line formation region of 2800 K, which is close to our chromospheric temperature minimum. These water lines are therefore formed in the lower chromosphere, far below the Hα line core. We therefore speculate that the different broadening velocities for the photospheric or lower chromospheric lines, and for the Hα line core (which forms higher and over a larger fraction in the chromosphere), could result in part from differences in the projected rotational velocity between their mean formation heights. The higher value for the latter would then point to the corotation (or rigid rotation) of the stellar chromosphere rather than a Keplerian rotation.

It has been known for some time that the UV spectrum of α Ori is rather atypical of (other less-luminous) late-type stars (Edmunds 1997). Carpenter et al. (1994) pointed out from Cycle 0 GHRS spectra of 1991 that the "UV continuum" is a true stellar continuum, which appears to originate from the chromosphere at temperatures ranging from 3000 to 5000 K. The large contribution of chromospheric emission below 3000 Å is also evident from our spectral synthesis. Unlike the optical spectra, for which we achieve almost perfect fits over wide spectral ranges, such fits to near-UV STIS spectra are of surprisingly poor quality. When the chromospheric model is not included in the radiative transfer, the majority of photospheric UV opacity results from SiO. No unblended atomic absorption cores could be isolated, and our synthetic spectrum only occasionally matches some deep and broad absorption blends seen in these spectra. This points to a strong emission background that significantly affects the observed UV fluxes. Since our photospheric model provides a mean absolute flux level at the SED maximum (near 8000–9000 Å), which is $\sim 10^7$ times stronger than the computed flux near 2000 Å, a weak emission background from the chromosphere can provide the major flux contribution and results in (undereddened) near-UV mean intensity levels of 2–5 10^{-12} ergs cm^{-2} s^{-1} Å^{-1} sr^{-1}. Note, however, that UV flux changes are observed in FOC images simultaneously obtained with the STIS spectra of 1998–1999. UV brightness changes are also seen in some earlier UV images (for a discussion, see Dupree et al. 1999). However, significant flux changes in the near-UV continuum of the four STIS spectra

TABLE 2

SEMIEMPIRIC MODEL ATMOSPHERES OF BETELGEUSE

Layer Number (1)	Height[a] (cm) (2)	T_{96} (K) (3)	T_{93} (K) (4)	N_e^{96} (cm^{-3}) (5)	N_e^{93} (cm^{-3}) (6)	V_{turb} (km s^{-1}) (7)	V_{92}[b] (km s^{-1}) (8)	V_{98}[b] (km s^{-1}) (9)
1	4.53580E+14	2584.3	2984.3	0.07290E+05	0.09290E+05	2.0	−3.6	5.0
2	4.03445E+14	3521.2	3721.2	0.50980E+05	0.70980E+05	7.0	−3.6	5.0
3	3.53128E+14	4518.2	4718.2	0.55450E+06	0.65450E+06	12.0	−3.5	5.0
4	3.09249E+14	4615.2	5015.2	0.33190E+07	0.53190E+07	15.0	−3.5	5.0
5	2.50000E+14	4914.2	5214.2	0.44290E+07	0.19290E+08	17.0	−3.5	5.0
6	2.02980E+14	4932.3	5332.3	0.77890E+07	0.30890E+08	19.0	−3.5	5.0
7	1.50000E+14	5043.5	5443.5	0.94596E+07	0.28596E+08	19.0	−3.5	5.0
8	1.13245E+14	5035.3	5335.3	0.12990E+08	0.28990E+08	19.0	−3.5	5.0
9	7.00000E+13	5034.3	5234.3	0.23595E+08	0.28595E+08	19.0	−3.1	5.0
10	3.28238E+13	5046.3	5146.3	0.28790E+08	0.29790E+08	18.0	−2.5	5.0
11	1.39298E+13	4933.2	5033.2	0.30090E+08	0.30090E+08	14.0	−1.5	4.0
12	8.60309E+12	4570.2	4570.2	0.40940E+08	0.34940E+08	11.0	−1.2	4.0
13	8.17171E+12	4077.4	4077.4	0.44180E+08	0.38180E+08	11.0	−0.9	4.0
14	7.82590E+12	3595.0	3595.0	0.55630E+08	0.55630E+08	11.0	−0.7	3.0
15	7.12864E+12	3013.1	3013.1	0.66920E+08	0.66920E+08	8.0	−0.5	3.0
16	5.95591E+12	2931.6	2931.6	0.68040E+08	0.68040E+08	7.0	−0.3	3.0
17	5.17604E+12	2850.3	2850.3	0.70570E+08	0.70570E+08	6.0	−0.2	3.0
18	4.74151E+12	2768.9	2768.9	0.75070E+08	0.75070E+08	4.0	−0.1	3.0
19	4.38919E+12	2787.3	2787.3	0.80790E+08	0.80790E+08	3.0	0.0	3.0
20	4.04284E+12	2805.3	2805.3	0.83000E+08	0.83000E+08	2.0	0.0	3.0
21	3.70260E+12	2823.0	2823.0	0.82060E+08	0.82060E+08	2.0	0.0	3.0
22	3.36907E+12	2840.5	2840.5	0.83440E+08	0.83440E+08	2.0	0.0	3.0
23	3.04251E+12	2858.1	2858.1	0.87660E+08	0.87660E+08	2.0	0.0	3.0
24	2.72314E+12	2875.9	2875.9	0.85400E+08	0.85400E+08	2.0	0.0	3.0
25	2.41149E+12	2894.0	2894.0	0.10750E+09	0.10750E+09	2.0	0.0	3.0
26	2.20063E+12	2812.5	2812.5	0.13480E+09	0.13480E+09	2.0	0.0	3.0
27	2.03474E+12	2831.6	2831.6	0.16860E+09	0.16860E+09	2.0	0.0	3.0
28	1.87220E+12	2851.3	2851.3	0.21010E+09	0.21010E+09	2.0	0.0	3.0
29	1.71282E+12	2871.7	2871.7	0.26110E+09	0.26110E+09	2.0	0.0	1.0
30	1.55693E+12	2892.6	2892.6	0.32340E+09	0.32340E+09	2.0	0.0	1.0
31	1.44284E+12	2814.1	2814.1	0.39900E+09	0.39900E+09	2.0	0.0	1.0
32	1.35023E+12	2836.0	2836.0	0.49070E+09	0.49070E+09	2.0	0.0	1.0
33	1.25977E+12	2858.3	2858.3	0.60110E+09	0.60110E+09	2.0	0.0	1.0
34	1.17118E+12	2881.0	2881.0	0.73370E+09	0.73370E+09	2.0	0.0	1.0
35	1.08448E+12	2903.8	2903.8	0.89230E+09	0.89230E+09	2.0	0.0	1.0
36	9.99654E+11	2927.0	2927.0	0.10820E+10	0.10820E+10	2.0	0.0	1.0
37	9.16439E+11	2950.5	2950.5	0.13070E+10	0.13070E+10	2.0	0.0	1.0
38	8.34767E+11	2974.4	2974.4	0.15760E+10	0.15760E+10	2.0	0.0	1.0
39	7.54706E+11	2999.1	2999.1	0.18980E+10	0.18980E+10	2.0	0.0	1.0
40	6.76122E+11	3024.6	3024.6	0.22840E+10	0.22840E+10	2.0	0.0	1.0
41	5.99081E+11	3051.5	3051.5	0.27490E+10	0.27490E+10	2.0	0.0	1.0
42	5.23650E+11	3080.2	3080.2	0.33160E+10	0.33160E+10	2.0	0.0	1.0
43	4.49831E+11	3111.3	3111.3	0.40130E+10	0.40130E+10	2.0	0.0	1.0
44	3.77890E+11	3145.6	3145.6	0.48850E+10	0.48850E+10	2.0	0.0	1.0
45	3.08097E+11	3184.2	3184.2	0.59960E+10	0.59960E+10	2.0	0.0	1.0
46	2.40854E+11	3228.3	3228.3	0.74440E+10	0.74440E+10	2.0	0.0	1.0
47	1.76698E+11	3279.5	3279.5	0.93730E+10	0.93730E+10	2.0	0.0	1.0
48	1.15964E+11	3339.0	3339.0	0.11980E+11	0.11980E+11	2.0	0.0	1.0
49	5.89887E+10	3407.6	3407.6	0.15520E+11	0.15520E+11	2.0	0.0	1.0
50	5.90558E+09	3486.4	3486.4	0.20300E+11	0.20300E+11	2.0	0.0	1.0
51	−4.36879E+10	3575.5	3575.5	0.26610E+11	0.26610E+11	2.0	0.0	0.0
52	−9.05970E+10	3677.2	3677.2	0.34740E+11	0.34740E+11	2.0	0.0	0.0
53	−1.36097E+11	3790.2	3790.2	0.44550E+11	0.44550E+11	2.0	0.0	0.0
54	−1.81731E+11	3915.8	3915.8	0.55710E+11	0.55710E+11	2.0	0.0	0.0
55	−2.29848E+11	4053.8	4053.8	0.67530E+11	0.67530E+11	2.0	0.0	0.0
56	−2.83401E+11	4206.3	4206.3	0.79450E+11	0.79450E+11	2.0	0.0	0.0
57	−3.45812E+11	4375.3	4375.3	0.91440E+11	0.91440E+11	2.0	0.0	0.0
58	−4.19833E+11	4563.7	4563.7	0.10620E+12	0.10620E+12	2.0	0.0	0.0
59	−5.05732E+11	4777.6	4777.6	0.13520E+12	0.13520E+12	2.0	0.0	0.0
60	−5.94316E+11	5023.0	5023.0	0.21000E+12	0.21000E+12	2.0	0.0	0.0
61	−6.71894E+11	5299.3	5299.3	0.39670E+12	0.39670E+12	2.0	0.0	0.0
62	−7.30346E+11	5619.0	5619.0	0.85920E+12	0.85920E+12	2.0	0.0	0.0
63	−7.70812E+11	5973.5	5973.5	0.19340E+13	0.19340E+13	2.0	0.0	0.0
64	−7.97857E+11	6372.1	6372.1	0.44110E+13	0.44110E+13	2.0	0.0	0.0

TABLE 2—*Continued*

Layer Number (1)	Height[a] (cm) (2)	T_{96} (K) (3)	T_{93} (K) (4)	N_e^{96} (cm^{-3}) (5)	N_e^{93} (cm^{-3}) (6)	V_{turb} (km s^{-1}) (7)	V_{92}[b] (km s^{-1}) (8)	V_{98}[b] (km s^{-1}) (9)
65	−8.14903E+11	6809.0	6809.0	0.98070E+13	0.98070E+13	2.0	0.0	0.0
66	−8.25976E+11	7251.3	7251.3	0.19870E+14	0.19870E+14	2.0	0.0	0.0
67	−8.33559E+11	7618.3	7618.3	0.33300E+14	0.33300E+14	2.0	0.0	0.0
68	−8.40069E+11	7874.6	7874.6	0.46110E+14	0.46110E+14	2.0	0.0	0.0
69	−8.46511E+11	8060.1	8060.1	0.57330E+14	0.57330E+14	2.0	0.0	0.0
70	−8.53222E+11	8233.8	8233.8	0.69380E+14	0.69380E+14	2.0	0.0	0.0
71	−8.60201E+11	8377.5	8377.5	0.80470E+14	0.80470E+14	2.0	0.0	0.0

[a] Atmospheric height above the stellar radius at $\tau_{5000} = 1$. Indices $_{93}$ and $_{96}$ refer to 1993 February and 1996 May.
[b] Chromospheric velocity structures for 1992 September and 1998 April.

are not evident. We attribute this difference to the small intrinsic variability at these wavelengths and the rather limited S/N ratios of these spectra. On the other hand, many prominent near-UV emission lines do show appreciable profile changes during this period, which can be linked with dynamics of the chromosphere, as is addressed in the next section.

4.2. Mg II *Resonance Doublet*

An important test for our mean chromospheric model is to properly fit opacity-sensitive line ratios such as the Mg II resonance doublet. On 1998 April 1 we observed these lines with very high resolution ($R \sim 114{,}000$) in order to resolve their detailed substructure and blends. The intensity maximum of their emission components (*bold solid lines* in Figure 5 are shown for scan peakup position) exceeds the background level by a factor of ~ 15. The good signal with respect to the chromospheric emission background renders them suitable for detailed spectral modeling purposes. Their central scattering cores, however, are clearly intensity saturated, which discards them for accurate measurements of changes in Doppler velocity of the scattering material. For the latter, we will further consider Si I resonance emission lines with unsaturated self-absorbed cores. The Mg II lines

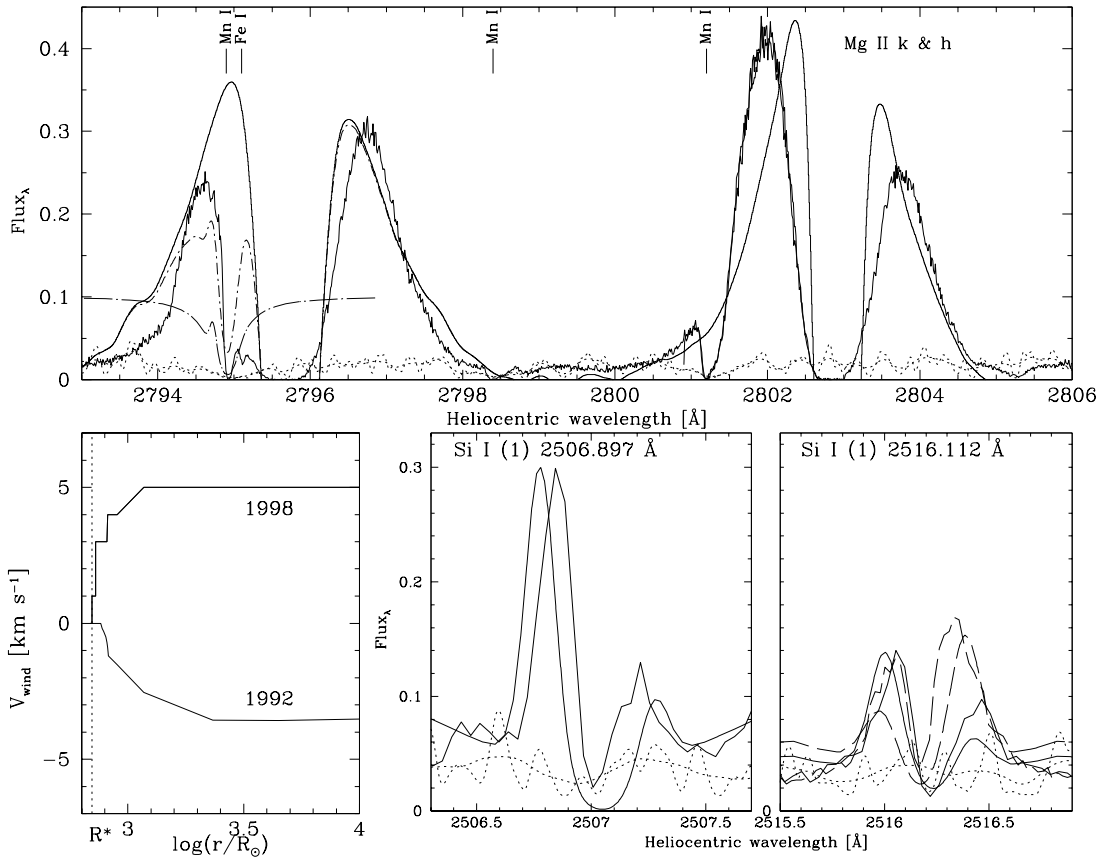

FIG. 5.—*Upper panel:* Detailed NLTE spherical radiative transfer calculations (*thin solid line*) with our chromospheric model fit the Mg II doublet observed at disk center with STIS in 1998 April with high dispersion (*bold solid line*). We compute a strongly self-absorbed Mn I λ2794.817 resonance line (scaled *thin long-dash–dotted line*) that distorts the blue k component and reproduces the steep edge after convolution (*thin short-dash–dotted line*). *Lower panels:* Best fits (*thin lines*) to unblended Si I resonance lines constrain the chromospheric velocity structure to inflow in 1998 April (*solid lines*) and outflow in 1992 September (*dashed lines*). The computed (and broadened) photospheric background is shown by the dotted lines. The computed velocity structures for both dates are shown in the left-hand panel.

are computed with SMULTI for a six-level model atom and iterated for seven line transitions. As for the Balmer lines, our calculations resolve both lines at 200 frequency points. In the upper panel of Figure 5, we show that the mean chromospheric model reproduces their relative intensities and also matches their different line widths (*thin solid lines*). Since the oscillator strength of the *k* line is twice as large as that of the *h* line, we compute in plane-parallel geometry with MULTI (Carlsson 1986) that the former is stronger than the latter, contrary to what is observed. We find that effects of spherical geometry cause the intensity of their emission-line components to nearly equalize because the central depression in the scattering core can drop to zero flux (to below the emission level of their broad wings). Such strongly self-absorbed cores cannot be computed in plane-parallel geometry and provide line half-widths too large by several factors. This unobserved broadness results because light rays that escape a flat slab of gas under large position angles must travel a larger distance through the hotter chromosphere (adding extra thermal broadening) than when passing through a curved chromosphere. In the latter case, these rays escape earlier from the chromosphere and therefore become also less broadened by microturbulence.

In a study of *IUE* spectra of high-luminosity cool stars, Robinson & Carpenter (1995) showed that the weakness of the blue emission component of the *k* line with respect to that of the *h* line in α Ori is rather uncommon among Ib stars (such as σ CMa or ε Peg). They also found a number of systematic, yet unexplained, differences in these line wings of their sample. However, similar as for the hybrid-chromosphere stars (Hartmann et al. 1985; Brown et al. 1996), a high-speed (chromospheric) wind in our radiative transfer would match this weakness of the blue *k* wing of α Ori but does not reproduce the high intensity observed in the blue *h* wing. Such a high-speed optically thick wind turns the computed blue *h* wing nearly equally weak as that of the *k* line and does not explain the observed component asymmetry. Neither could we attribute this asymmetry to a higher optical depth of the *k* line, whereby it would become more attenuated than the *h* line in this wind. The bulk of the emission in these resonance lines originates from deep chromospheric levels, as is shown in the upper panel of Figure 6. The contribution functions to the relative line intensity (wavelength integrated over the entire profile) show only a somewhat larger contribution to the *k* line for the outermost (very low density) layers of our chromospheric model. The *k* scattering core therefore enhances somewhat over that of the *h* line (i.e., compare the width of both cores in Fig. 5), but this effect is not able to produce the observed asymmetry. On the other hand, the integrated

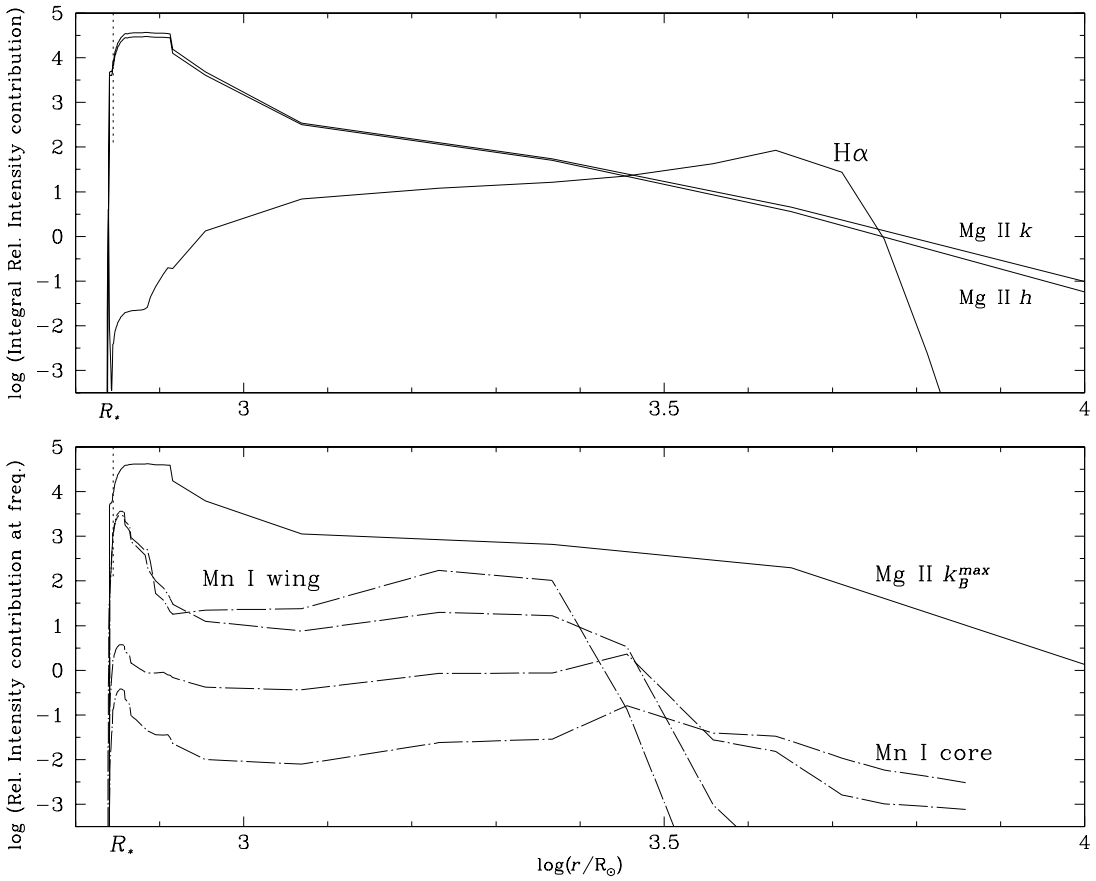

FIG. 6.—*Upper panel:* Wavelength integrated contribution functions to the relative line intensity of Hα, Mg II *h* and *k* are shown on a logarithmic scale. Emission components of the Mg II resonance doublet emerge mainly from the deeper chromospheric layers. Hα absorption with high lower energy level forms mainly in the middle (line wings) and upper chromosphere (line core). *Lower panel:* The contribution functions to the relative intensity of the Mn I line at 2794.8 Å are shown for four wavelengths (*dash-dotted lines*) from the line wings to the core. Its self-absorbed core emerges from the upper chromosphere, above the layers where the contribution function at the wavelength of the intensity maximum in the blue Mg II *k* component peaks. The vertical dotted line is drawn at the photospheric radius R_*.

contribution function of Hα shows that this absorption line is completely formed (including its wings) in the stellar chromosphere.

To estimate the possible contribution of interstellar Mg II, we compared equivalent-width and FWHM values of interstellar Mg II lines observed for two hot stars toward α Ori. Trapero et al. (1996) observed high-velocity interstellar Mg II absorption components in GHRS spectra of 23 Ori, a B-type star at a distance of 450 pc and $\sim 9^\circ$ in the sky from Betelgeuse. For the interstellar absorption lines at low velocity, we measure equivalent widths of ~ 350 mÅ and FWHM values that do not exceed 0.3 Å. We determine the equivalent widths for the self-absorptions in the Mg II doublet, observed with high-resolution in 1998 April for α Ori, with respect to a Gaussian emission profile that fits their broad line wings. Hence, the integrated self-reversal of the *k* line yields an equivalent width of 1525 ± 100 mÅ and a value of 1130 ± 100 mÅ for the *h* line. These high-resolution observations indicate that possible contributions from interstellar absorption in the broad self-reversed Mg II cores (with FWHM $\simeq 1$ Å) of α Ori are expected to remain below 25%. Smaller equivalent-width and FWHM values are observed in medium-resolution STIS spectra of GD 71, a white dwarf at a distance of 40–50 pc, $\sim 8.5^\circ$ near Betelgeuse. Its spectrum does not reveal interstellar absorption components that are clearly separated from low-velocity interstellar Mg II *k* and *h* absorption lines, as in 23 Ori, but we measure that the equivalent width and FWHM values for latter lines are, respectively, 89 mÅ and 0.21 Å, and 52 mÅ and 0.23 Å. These small values also suggest that interstellar contributions remain negligible in Betelgeuse's broad and saturated Mg II line cores. This is further supported by the profiles computed in Figure 5 with our chromospheric model for this doublet, which provide zero flux self-reversals and an overall shape of their emission components that strongly matches our observations.

A very important property of Betelgeuse's Mg II lines is that the ratio of the emission peaks of the *h* line appears to change drastically over long periods of time, whereas that of the *k* line remains nearly fixed. Disk-integrated *IUE* spectra show that the blue *h* component was weaker than the red before 1990, whereafter these intensities reversed. For instance, Kondo et al. (1972) and Bernat & Lambert (1976) also observed a *k* line ratio comparable to current observations, but instead with a rather symmetric *h* line. Furthermore, our spatially resolved scan with STIS across the chromospheric disk shows appreciable changes in the intensity ratio of this line, as was already noticed in the GHRS scans of 1995 March (Uitenbroek, Dupree, & Gilliland 1998). However, changes in the component ratio of the *k* line are much harder to detect at the five scan positions with the STIS high-resolution grating of 1998 April. All these observations seem to indicate that the *h* line displays a direct sensitivity to changes in the chromospheric velocity field where the central scattering core of the line forms. It could therefore display the actual chromospheric dynamics, whereas the *k* line suffers heavily from additional (and persistent) opacity blanketing of a different origin.

The *k* line contains blends of Mn I (UV 1) at 2794.817 Å and Fe I (UV 3) at 2795.006 Å, which are both sharply resolved in the STIS spectrum of Figure 5. Unlike the Fe I absorption core, the Mn I core drops to zero intensity and produces by its blue wing profile the very steep edge in the blue *k* component. Note that such a steep emission edge is absent in the narrower *h* core. Bernat & Lambert (1976) suggested that a cool circumstellar shell with low excitation temperature (1000 K) for both lines could contribute to the strong asymmetry observed in the *k* line. But they also found that the amount of absorption by scattering in this shell (atop of the chromosphere) would be insufficient to provide this asymmetry (especially for α Sco). On the other hand, based on their high-resolution GHRS spectrum, Robinson & Carpenter (1995) argued that both blends are much too narrow to account for this. The next section will demonstrate, based on our NLTE radiative transfer calculations, that the apparent narrowness of the Mn I line can be reconciled with a scattering core, which is, however, of chromospheric origin.

4.3. Ca II *Infrared Triplet*

The chromospheric parameters can be further tested by fitting the Ca II triplet cores in the near-IR UES spectra. At a resolution of 50,000, none of these lines showed signs of core emission, as was already noticed by Weymann (1962). SMULTI fits of these Ca II lines with our photospheric and chromospheric model do produce a small amount of filling in of the deep photospheric core at 8662 Å, but no prominent central emission reversal could be produced after smoothing and rescaling to the molecular background. The predicted width of the broad damping wings also nearly fits the observed wing profiles. Since we apply chromospheric microturbulences ranging to 19 km s^{-1}, this supports the remark of Hartmann & Avrett (1984), who noted that their wave-driven broadening velocities, below 11 km s^{-1}, must be increased by a factor of 2 for better agreement with observations. Furthermore, their predicted line profiles did produce an emission core reversal in Ca II 8542 Å, which we attribute to overestimated kinetic temperatures, ranging to 7100 and 8050 K near 4 R_*, in their theoretical models. Our semiempirical line-profile modeling requires chromospheric temperatures not exceeding 5500 K. Wirsich (1988) adopted $T_{\max} = 6048$ K and pointed out that insufficient hydrogen ionization occurs for lower temperatures. These lower values are consistent with the spectral modeling by Basri, Linsky, & Erikson (1981), but they computed Ca II and Mg II lines in plane-parallel geometry.

4.4. *Partial Frequency Redistribution Modeling*

We have checked α Ori's chromospheric model for possible effects from partial frequency redistribution (PRD) in this extended atmosphere. The full frequency dependency of the line source function is not incorporated by solving the radiative transfer equation with SMULTI, which considers complete frequency redistribution (CRD). Additional computations, which include PRD and spherical geometry, have been carried out with PANDORA by Dr. E. Avrett (2000, private communication). These calculations yield no difference in the emergent line flux for Hα, compared with our CRD calculations, by which we constrain the chromospheric conditions. This is because the core of this Balmer absorption line is formed entirely in the upper chromospheric layers, where its line source function decreases monotonically outward. Possible PRD effects in the wings of the very optically thick Lyα emission line remain limited because these line wings are formed mainly deeper down, near the chromospheric temperature rise (similar to the Mg II doublet lines in Fig. 6). The line source function in the Hα line core and the wings can therefore be treated as fre-

quency independent and can be represented by a single monochromatic line source function. For example, in the Sun there is no difference between PRD and CRD, because the Hα wings are collisionally redistributed (Hubeny & Lites 1995). More generally, we note that important differences between CRD and PRD calculations for pure absorption lines have not been demonstrated to date.

Figure 7 shows the Ca II K line observed on 1985 September 25 (*thick solid line*) at Whipple Observatory and on 1998 October 11 with NOT-SoFin (*thick dash-dotted line*). In 1985, its long-wavelength emission component was stronger than in the spectrum of 1998, but the S/N of the latter observation was lower. The (unbroadened) background computed with the photospheric model is drawn by the dotted line. This LTE modeling matches the shape of the very wide K absorption line wings but does not account for the strongly self-absorbed central emission reversal produced by the stellar chromosphere. The line profile computed with the model chromosphere in CRD with SMULTI is shown by the thin dashed line. It matches the width and depth of the self-reversal but produces emission wings that are too broad. These observed narrower widths can be accounted for by including PRD in the radiative transfer. Partial frequency redistribution computations, carried out in spherical geometry by Dr. H. Uitenbroek (2000, private communication), with our photospheric/chromospheric model are shown by the thin solid line. They appreciably improve the overall fit to the Ca II K line profile by redistributing emission flux from the broad line wings to the central emission core. These complex radiative transport calculations, however, are carried out for hydrostatic equilibrium and therefore do not yield the observed intensity differences in the maxima of the emission components, which result from the chromospheric dynamics (§ 6). These

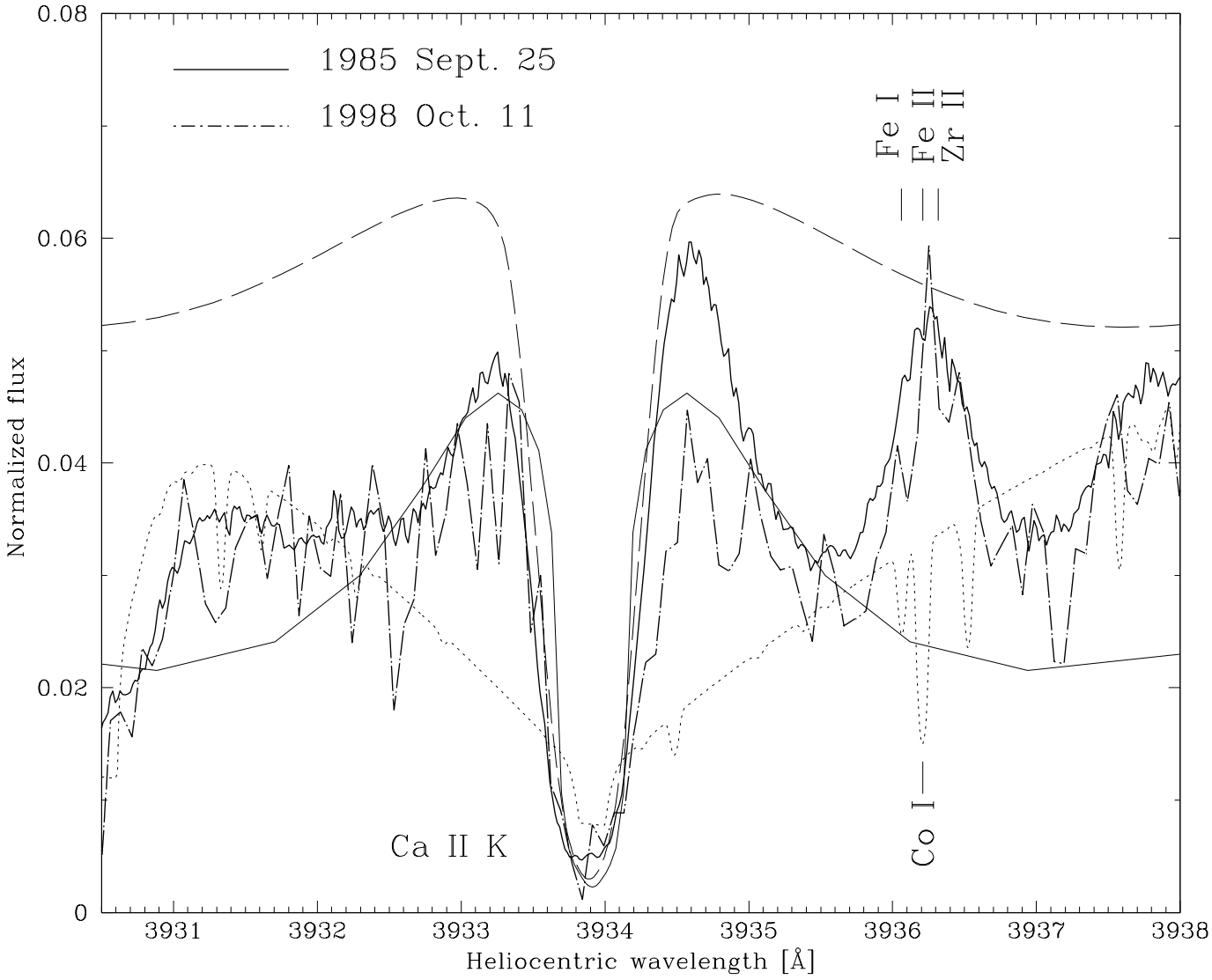

FIG. 7.—Two Ca II K line profiles observed in 1985 September (*bold solid line*) and 1998 October (*bold dash-dotted line*) display small variations in their central emission reversals emerging from the stellar chromosphere. A best fit with the chromospheric model determined from Hα for this work is obtained with radiative transfer in spherical geometry, which incorporates partial frequency redistribution (*thin solid line*). The effects of PRD in this broad absorption line improve the widths of the central emission components, which are too broad when assuming complete redistribution (CRD) with SMULTI (*thin dashed line*). The model reproduces the width and depth of the observed self-absorption profile both for PRD and CRD. The dotted line is computed in LTE without the chromosphere. This photospheric model matches the shape of the broad absorption wings of the Ca II doublet lines. Note the strong chromospheric emission feature in the red K wing, which results mainly from Fe II (see text).

variations, however, remain limited in the Ca II K line, and the PRD fit confirms the required chromospheric conditions we constrain from CRD fits to Hα. Note further the strong emission feature near 3936 Å in the red wing of this broad absorption line, which is also visible in Figure 1 of Basri, Linsky, & Erikson (1981). Our spectral synthesis identifies the strongest photospheric absorption line at these wavelengths as a hyperfine splitting band of Co I lines. The emission maximum in the stellar rest frame coincides with a chromospheric Fe II emission line at 3935.962 Å, which is blended with emission from Fe I λ3935.813 and Zr II λ3936.067.

Similar PRD calculations for the Mg II doublet also yield somewhat narrower lines than for CRD. The CRD profiles computed with SMULTI appear in better agreement with our observations than the full PRD treatment, which could indicate that collisional redistribution is important in the wings of these strong optically thick emission lines. But in these lines, the effects of spherical geometry from Betelgeuse's extended chromosphere are far more important because it considerably narrows the emergent line width compared to plane-parallel geometry (see § 4.2). Note, for instance, that Singh (1994) has pointed out that the differences derived with (angle-averaged) PRD and for CRD are much smaller in expanding spherical symmetric atmospheres than derived for plane-parallel geometry. Thus the PRD calculation of line profiles of Hα and Ca II confirm our model atmosphere.

4.5. *Mid-Infrared and Radio Data*

Skinner et al. (1997) have argued from SED fits to radio and mid-IR data that high temperatures of 9000 K are required for the inner few photospheric radii. For this high temperature and comparable electron densities, we compute that the Hα core would become too shallow for our observations because the chromospheric hydrogen ionization fraction becomes too large. It is possible that these differences result from asymmetries in a very extended Hα chromosphere, as was inferred from speckle images in the Hα line core by Hebden, Eckart, & Hege (1987). Therefore, the assumption of a homogeneous chromosphere is important for this SED modeling. A highly clumpy medium would allow for somewhat higher electron densities in these clumps, without affecting the resulting SED or visibility curves (Skinner et al. 1997). Probably, this could lower their (mean) temperature maximum to our value.

With the VLA, Lim et al. (1998) measured (6 cm) radio brightness temperatures (T_b) decreasing outward to 1370 ± 330 K at a distance of $\sim 7\,R_*$. If these disk-averaged low brightness temperatures correspond with the same kinetic gas temperature T (note T_b is an optical depth weighted integral of T; i.e., Dulk 1985), it would imply cool gas coexisting with the hot chromospheric gas that produces the Hα absorption and the near-UV emission lines. They estimate that the cool gas is more abundant by 3 orders of magnitude because below 4000 K electron-neutral radio absorption is smaller by this amount than electron-ion free-free absorption. The formation of the Hα absorption core, extending to 150 mas, could therefore occur in confined regions (or pockets) of hotter and denser partially ionized chromospheric gas, immersed in a cool stellar envelope of dominantly neutral hydrogen. However, the spatially resolved scans with STIS do not show large intensity fluctuations in bright chromospheric emission lines like Mg II *h* and *k* near the limb of the UV disk, which would point directly to the existence of such hot pockets with sizes larger than the aperture of 25 by 100 mas. Simultaneous FOC imaging (Dupree et al. 1999) rather reveals continuum brightness patterns preferentially seen near the middle of the UV disk, within ~ 30 mas of intensity peakup (see Fig. 1).

We therefore consider our semiempirical models as a "mean" condition of α Ori's chromosphere, which is required to constrain the detailed velocity structure and to model its dynamical changes observed over time.

5. MODELING THE CHROMOSPHERIC VELOCITY STRUCTURE

To this end, we introduce a velocity structure for the radiative transfer through the chromospheric model. The dependence of velocity with height is constrained semiempirically from best fits with SMULTI to selected chromospheric emission lines. For this purpose, we consider two double-peaked Si I emission lines at 2506.897 and 2516.112 Å. Spectral synthesis calculations indicate that these resonance lines are unblended as their photospheric background does not display broad saturated absorptions. The dotted lines in Figure 5 are the high-resolution (computed and broadened) photospheric spectrum. This background is computed in LTE with the purely photospheric model. It also serves as a scaling offset for the separate atomic NLTE calculations, which include both the photospheric and chromospheric model. For example, in the upper panel of Figure 5, the broad photospheric absorption profiles of the three Mn I lines at 2794.817, 2798.269, and 2801.081 Å are clearly visible in this computed background. Here, we have "switched off" the photospheric absorption contributions of the Mg II lines (producing very wide damping wings) since their photospheric portions are already incorporated in the Mg II NLTE calculations.

We compute with SMULTI that the intensity ratios of the double-peaked Si I lines (observed in 1998 April; *bold solid lines in the lower panels* of Fig. 5) are best fit for an inward decelerating chromospheric velocity structure (shown in the lower left panel and tabulated in col. [9] of Table 2). The inflow velocity in the outer layers does not exceed 5 km s^{-1} and decreases monotonically toward the photosphere. We solve a Si I model atom with 12 energy levels, for six lines and nine fixed transitions (H. Uitenbroek, 1999, private communication) at 100 frequency points. The emission profiles we compute with this velocity structure (*thin solid lines*) match the observed line widths, although the scattering core of the stronger transition at 2506 Å is somewhat too deep. This best fit is obtained after degrading the theoretical profiles with the instrumental resolution (30,000) and applying a macrobroadening and $v \sin i$ of 9 ± 1 km s^{-1}. We also choose to model these Si I lines because this atomic structure is rather simple compared with Fe II. Our STIS spectra of α Ori display many subordinate Fe II lines (e.g., see the identification list of Brandt et al. 1995) with a stronger blue emission component, similar as that for the Mg II *h* line.

This chromospheric velocity structure reproduces the component ratio of the Mg II *h* line, but for the *k* line profile, we also consider the chromospheric Mn I blend. We converge with SMULTI a twelve- level Mn I model atom for six lines and 12 fixed transitions. In the upper panel of Figure 5, we overplot the scaled profile of this line at 2794.817 Å (*thin*

long-dash–dotted line). The infalling chromosphere produces a strongly self-absorbed emission core for this resonance transition, yielding an apparent inverse P Cygni type profile (note that this analogy refers only to shape, since the formation of actual P Cygni profiles does not require a stellar chromosphere as their emission wings emerge from a cooling and expanding wind outside the line of sight). When the Mn I line is shifted to the stellar rest frame, and its background is scaled to the computed blue emission component of the *k* line, we find that the resulting line width (again after degrading with the instrumental resolution and macrobroadening) compares well with the observed Mn I core. This scaling procedure is justified since we compute that its scattering core forms mainly in the upper chromosphere. The lower panel of Figure 6 shows how the contribution functions to the relative intensity at a frequency in this line form gradually higher in the chromosphere by moving from the line wings toward the core, whereas the contribution function to the intensity maximum of the blue Mg II *k* component peaks in the deeper chromosphere. The resulting convoluted profile (*short–dash-dotted line in the upper panel* of Fig. 5) of the blue *k* component matches its observed steep edge, and the Mn I core can clearly account for the major part of missing opacity in this component. It thus follows that the Mn I blend is not of photospheric origin but is in fact a deep and narrow scattering core emerging from the chromosphere. Similarly, we think that a modeling of the weaker 2795 Å Fe I blend, formed at much smaller optical depths (see Carpenter & Robinson 1997), can account for the remainder of missing opacity in the blue *k* component and also contribute to its permanent weakness. This interpretation is further supported by additional tests that assume more complex radial velocity structures in the chromosphere but that could not match the observed Mg II asymmetry. When inserting velocity structures that accelerate outward in the outermost chromospheric layers above $\log (r/R_{\odot}) = 3.3$, on top of a collapsing inner velocity structure, the intensity of the blue *k* component could be matched but without fitting the much stronger blue *h* component. This reversed ratio for the emission components observed in the Mg II *h* and *k* lines cannot be modeled with complex dynamic radial velocity structures. It results from the limited differences in the contribution functions shown in Figure 6 for both lines in the outermost chromospheric layers of our models.

Gilliland & Dupree (1996) suggested that this Mn I line originates in the circumstellar environment because its equivalent width varies with scan position on the chromospheric disk, whereas the interstellar Mg II (λ2795) line remains constant in the comparison star η UMa. The next section provides further indications that this deep line core is not of interstellar origin in α Ori. This follows from Doppler displacements we observe over time in this scattering core that are identical to those seen in our STIS spectra for the cores of many other self-absorbed emission lines, which form in a dynamical chromosphere.

6. CHROMOSPHERIC DYNAMICS

In Figure 8 we show line-profile changes observed between 1992 September and 1999 March. These Doppler shifts in Fe II λ2392 and Si I λ2516 are typical for most emission lines in the near-UV. Their absolute wavelength calibration is discussed in § 2.1, with errors typically below 1 pixel $\simeq 5$ km s^{-1}. We detect redshifts by $\sim +8$ km s^{-1} in their scattering cores between 1998 January and September. This Doppler displacement of these self-absorbed cores slightly enhances the intensity of the short-wavelength emission component (*short-dash–dotted lines*), which results from an average downflow of the scattering material in the line of sight. In the spectrum of 1999 March, however, the cores shifted to the shorter wavelengths again by ~ 4 km s^{-1}, yielding a strong intensity enhancement in the long-wavelength emission component (*long dashed lines*). Changes of asymmetry in this Fe II line were noticed already by Brandt et al. (1995) from comparisons of *IUE* and GHRS spectra. But its correlation with the small shifts detected in the central scattering cores is now evident from our STIS monitoring. We find that the mean chromospheric downflow in these lines decelerated during ~ 9 months (with the chromospheric velocity structure of Fig. 5), and these velocity fields were expanding thereafter.

Doppler shifts for the Mg II resonance doublet, however, are much harder to assess because these broad cores are strongly intensity saturated and both short-wavelength components appear mutilated by chromospheric Mn I blends. But the GHRS spectrum of 1992 clearly shows a much stronger long-wavelength component for the doublet (after a rescaling of the flux for the GHRS field of view to the aperture of the STIS spectra). This is also the case when comparing with the summed spectrum taken over the three central exposures in the high-resolution STIS scan of 1998 April. This summed spectrum covers 200 mas by 189 mas, which compares to the 200 mas by 200 mas field of view of the GHRS. The latter observation is therefore linked with a large redshift by ~ 0.3 Å of the intensity maximum in the long-wavelength components between 1992 and 1998. The smaller width in the self-absorption cores of 1992 results from changes in the dynamics of the chromosphere over time. In 1992, the chromosphere was strongly expanding, causing the line bisector of these scattering cores to displace blueward. This could be linked with lower densities in the upper chromosphere which produce narrower scattering cores. Similar (but lesser) redshifts by 10–20 km s^{-1} of the long-wavelength component maxima are also observed during this period in many weaker near-UV emission lines. For all these spectra, we measure identical Doppler shifts for the Mn I 2794 Å core, which weakens the Mg II *k* component, lending further support for its formation in the dynamic chromosphere we modeled in § 5.

We choose to model the shape of neutral silicon lines because they appear uncontaminated by interstellar absorption. Higher ionization stages of silicon in the UV are found in the interstellar medium (ISM) toward the Orion OB1 association (i.e., Shull 1979). These low-ionization elements (Fe) become photoionized by the interstellar UV radiation field. Morton (1975) listed a very weak Si I λ2514.316 line in the spectrum of ζ Oph, a star known for having foreground ISM conditions favorable for producing neutrals and molecules. But the detection is not conclusive because of bad noise problems. Nevertheless, modeling these Si I lines is complicated by fluorescing processes in α Ori's chromosphere. Carpenter et al. (1988) pointed out that Si I λ2516.1 is a fluorescent line the upper level of which is populated by the Fe II fluorescent line at 2506.8 Å pumping the Si I transition at 2506.9 Å. Therefore we constrain only the chromospheric velocity structure from these Si lines but not the thermodynamic conditions. The latter are based on absolute intensity and the line width

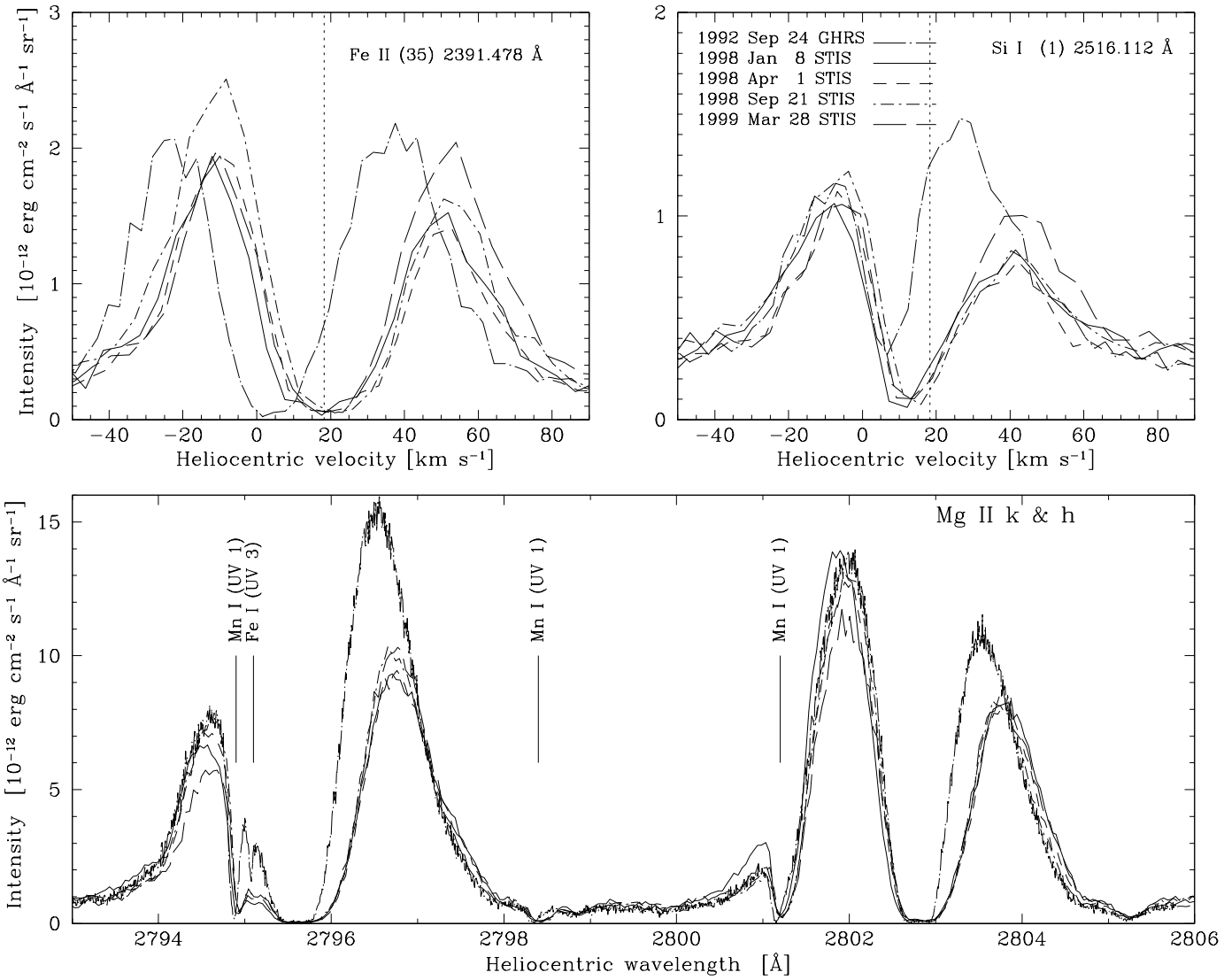

FIG. 8.—*Upper panels:* Numerous near-UV emission lines display redshifts in their scattering cores of $\sim +8$ km s^{-1} between 1998 January and September, indicating mean chromospheric inflow. The line patterns for different dates are indicated in the right-hand panel. The dotted vertical line denotes the *Hipparcos* transverse velocity of 18.27 km s^{-1}. Thereafter the cores shift blueward by 4 km s^{-1} and a clear strengthening of the long-wavelength emission component occurs (*long dashed lines*), indicating chromospheric upflows. In 1992 September, the intensity of many long-wavelength components was much stronger, as expected from faster upflow motions (*long dash-dotted lines*). *Lower panel:* This intensity enhancement in 1992 September was very strong in the Mg II doublet (*long dash-dotted line*), indicating a phase of global chromospheric expansion. Note the large redshift by $\sim +0.3$ Å of their red emission maxima between 1992 and 1998. The Mn I core that mutilates the blue *k* component shows the same Doppler shifts over time that are observed in many Fe II cores, which also points to its chromospheric origin.

of Hα and the relative intensity and total line widths of the Mg II doublet, together with the width of their self-reversals with respect to the latter. Also, the appreciable chromospheric background emission for these weaker Si I emission lines must be accounted for by a scaling factor.

In Figure 5, we introduce a monotonically outward accelerating chromospheric velocity structure to match the component intensity ratio of the Si I λ2516 line of 1992 (*bold dashed line in lower right-hand panel*). The best fit (*thin dashed line*) with our mean chromospheric model is obtained for a terminal velocity not exceeding 4 km s^{-1}. This maximum speed is reached within 3.6 R_* and remains subsonic since it is well below the isothermal sound speed of $\sim$7 km s^{-1} (for a mean atomic weight with solar abundance of $\mu = \mu_0/(1 + \bar{x}) = 1.26/1.35$, where $\bar{x}$ is the mean ionization fraction) at these heights. A steeper chromospheric wind structure or higher terminal velocities would suppress the blue component too much. The velocity structure with atmospheric height is listed in column (8) of Table 2. Although our α Ori spectra of 1998–1999 mostly display chromospheric downdrafts instead of expansion, this accelerating velocity structure in 1992 appears to be consistent with the notion by Harper (1996) that winds from cool giants reach at least half their terminal velocity, well within a stellar radius above the photosphere. Note that the "terminal velocity" considered here is for chromospheric outflow inside a dust cavity. Below, we discuss higher terminal velocities that are actually observed for the gas component of α Ori's circumstellar dust shell. Carpenter & Robinson (1997) detected in the scattering cores of 24 selected Fe II lines of α Ori a clear trend of increasing blueshift with increasing opacity or height. Hence, they directly

sampled this accelerating region in the (lower) chromosphere from rest to ~ 7 km s^{-1} for the GHRS spectrum of 1992.

These measurements, our STIS observations, and the present radiative transport modeling therefore strongly point to mass movements across the chromosphere that fall down and expand over time, with decelerating and accelerating wind structures. The temporal reversal from downflow to upflow is shown in Figure 9 for Fe II λ2868 (*lower panel*). The inversion of its component intensities indicates a reversal of these mass motions from chromospheric mean inflow to outflow after 1998 September 21. The spectra are spatially resolved but shown here at intensity peakup. On the latter observation date we observe that the ratio in the component intensities of certain lines can invert when scanning across the UV disk. This indicates mass movements streaming through the upper chromosphere in opposite directions in the line of sight, which we will discuss and model in a forthcoming paper. Such spatial inversions, however, are not clearly detected in the earlier raster scans of 1998 January and April, which display average downflows across the entire chromosphere.

Reversals of component ratios over time are detected between 1998 January and 1999 March in many other unsaturated scattering cores such as Al II] λ2669. In the upper panels of Figure 9 we compare the high-resolution profiles of 1992 (*thin solid lines*) and of 1998 April 1 (*bold solid lines*). The dash-dotted lines are also observed on the latter date but with the moderate resolution of the time sequences shown in the lower panels. It reveals that the degrading effect of instrumental broadening can affect the observed ratio of these component maxima. This effect is

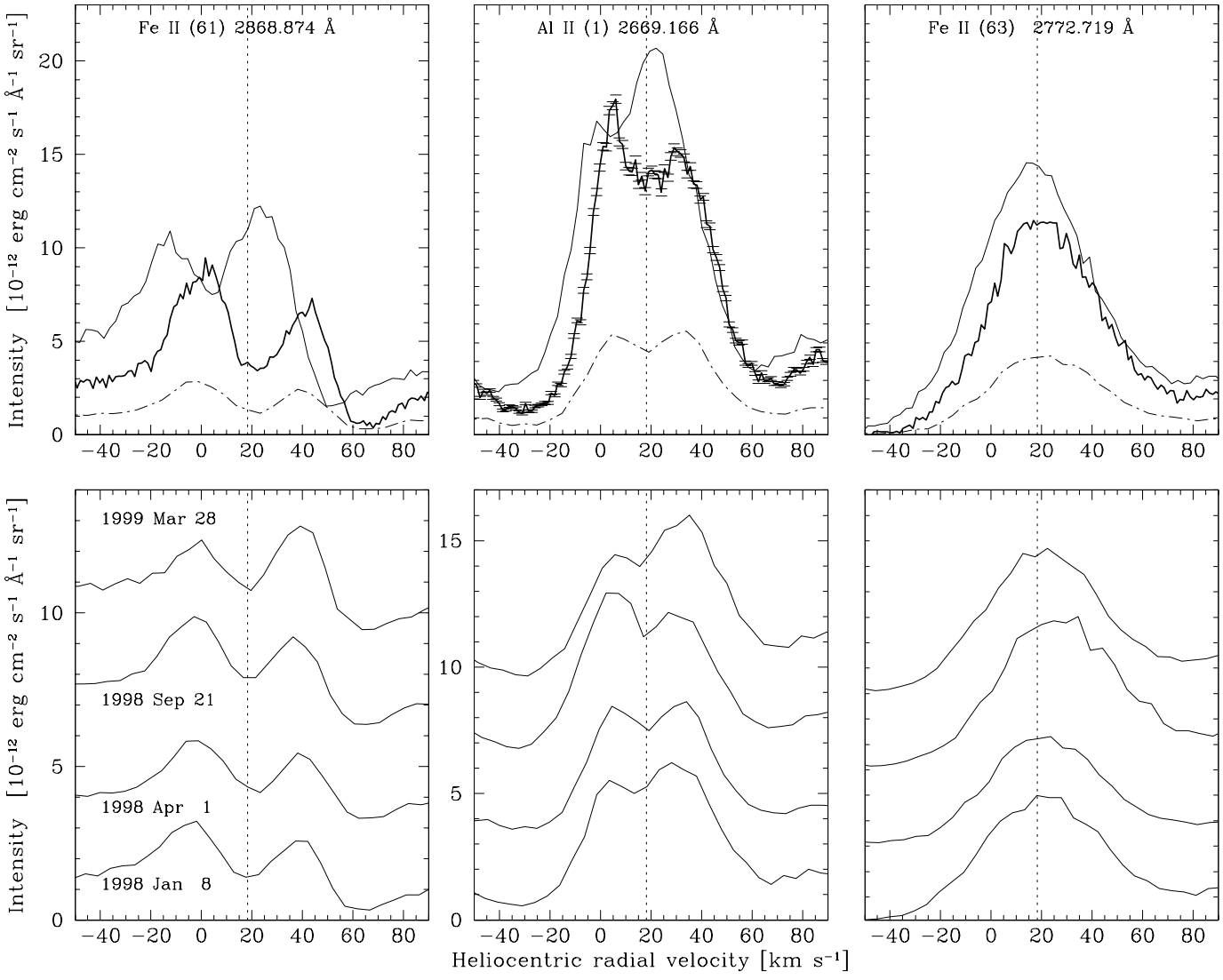

FIG. 9.—*Upper panels:* Comparison of chromospheric emission lines with unsaturated self-absorbed cores shows that the lines were broader in 1992 when the chromosphere was expanding (*thin solid lines*). In 1998 April, the blue emission component became stronger (*bold solid lines*), but the line width in the blue wing was smaller. The profiles of these lines, observed on the same date but with the smaller STIS aperture and medium resolution, are shown by the dash-dotted lines. They reveal that the degrading effect by the lower dispersion on the component ratios remains small if both emission maxima are well separated (≥ 30 km s^{-1}). Error bars in line fluxes for the high-dispersion Al II profile are plotted as provided by the STIS calibration pipeline. The short-wavelength maximum of this line is significantly stronger than the mean noise level. *Lower panels:* Time sequences of the lines in the upper panels (*left to right:* Fe II, Al II, and Fe II). Profiles are shifted upward with time. The time sequence of the Fe II λ2868 line shows how the chromosphere was collapsing in the mean formation region of its scattering core between 1998 January and September. Thereafter its emission maxima reverse, indicating mean chromospheric outflow. These profiles are spatially resolved and observed at intensity peakup of the UV disk (see text).

expectedly stronger for lines with smaller separation between the core maxima, such as the Al II line. But for most broad Fe II lines, having component separations exceeding 30 km s^{-1}, we find that the STIS observations with $R = 30{,}000$ do not bias these component ratios significantly. The blueshift measured in scattering cores of the disk-integrated GHRS spectrum of 1992 reveals a phase of global chromospheric expansion, which is evident by the much stronger intensity of the red component, found equally in many strong and weak permitted lines.

Careful comparisons of line shapes over time also reveal how the FWHM of these permitted emission lines was larger by $\sim$10 km s^{-1} in 1992. For example, Fe II λ2772 [with low log (*gf*) in UV multiplet 63] shows no detectable self-absorption core but was significantly broader then. This line peaks at the same systemic velocity of 1998 April, which gives confidence that our absolute wavelength calibrations are accurate. These variable emission line widths indicate that they are opacity sensitive. Temporal changes of line widths dominantly seen in the blue emission wing imply their formation in an optically thick dynamic wind. Variations of microbroadening or thermal conditions in a static chromosphere would rather result in a symmetric broadening.

For the expanding wind model of 1992, we compute a gas density of $\rho = 9 \times 10^{-17}$ gr cm^{-3} from our mean chromospheric model at the kinetic temperature maximum of $r = 5.2\ R_*$. Assuming spherically symmetric outflow at this radius, where the terminal velocity $v_\infty = 4$ km s^{-1} is reached, we compute a mass-loss rate in this phase of $5.7 \times 10^{-7}\ M_\odot$ yr^{-1} from $\dot{M} = 4\pi r^2 \rho v_\infty$, with $R_* = 700\ R_\odot$. This value is within the range of 4×10^{-7} to $2 \times 10^{-6}\ M_\odot$ yr^{-1} derived by Knapp, Phillips, & Huggins (1980) from the millimeter CO (2–1) emission line. This optically thin line shows, however, an expansion velocity for the cold circumstellar envelope of $\sim$15 km s^{-1}, which was also detected from a C I line by Huggins et al. (1994). The latter find good agreement with the $\dot{M}$-value of 2–6 $\times 10^{-6}\ M_\odot$ yr^{-1} of Bowers & Knapp (1987), who measured a half-power width of $\sim$16 km s^{-1} for the 21 cm H I line. Loup et al. (1993) estimated a CO mass-loss rate of $3.1 \times 10^{-7}\ M_\odot$ yr^{-1} for $d = 190$ pc and an expansion velocity of 13.6 km s^{-1}. For the more recent distance determination of 131 pc (ESA 1997), these values are not inconsistent with our $\dot{M}$-value from chromospheric modeling. However, the terminal velocity in the circumstellar gas shell is at least 3 times larger than during occasional phases of outflow we observe in the oscillating chromosphere. Perhaps larger velocities do occur in the stellar chromosphere, but the near-UV observations on the five dates discussed here did not capture them. It points to a possible different driving mechanism beyond the dust condensation radius R_c, i.e., by radiation pressure onto grains dragging the gas in the cold envelope to much higher velocities. This is also supported by the silicate dust emission feature at 9.7 μm observed between 1994 and 1996 by Monnier, Geballe, & Danchi (1998). Its unchanging intensity and shape is a signature of constant mass flux near R_c in an optically thin dust shell. We think that recurrent upflows by the chromospheric pulsations could then supply sufficient mechanical momentum for the gas to cross the inner dust cavity below $R_c \simeq 19\ R_*$, or $\sim$3 times the height of our model chromosphere. Here R_c is approximated with $(T_{\rm eff}/T_c)^2\ R_*$ (e.g., Habing 1996), similar as for early M-type AGB giants with dust condensation temperatures of $T_c \simeq 800$ K. The onset of effective dust formation of SiO takes place at gas temperatures below 750 K (Beck et al. 1992; Gail & Sedlmayr 1998). Model fits to the IRAS LRS 9.7 μm silicate feature by Skinner et al. (1997) suggest an inner dust shell radius of $\sim 34\ R_*$, corresponding to a dust temperature of 700 K. At larger distances, the temperature of the dust in thermal equilibrium decreases with $r^{-1/2}$. From mid-IR imaging, Rinehart, Hayward, & Houck (1998) obtain a grain dust color temperature of 460 $\pm$ 20 K, beyond 1″ from the star. Recently Justtanont et al. (1999) computed $\dot{M} \sim 5 \times 10^{-7}$ $M_\odot$ yr^{-1} (identical to our chromospheric mass-loss rate) from infrared fine structure [Fe II] and [Si II] lines formed within 20 R_*, inside the dust cavity. They adopt an outflow velocity of $\sim$2 km s^{-1} and compute a total gas mass in this volume of $10^{-4} M_\odot$ for radiative cooling in these lines. Since our mass-loss rate is an upper value (derived for a phase of outflow), at this rate it would take at least 200 yr to fully replenish this circumstellar gas volume. This dynamical timescale for the circumstellar gas envelope compares to a time of ca. 150 yr for a stationary wind of 2 km s^{-1} to cross 20 R_*. Figure 10 gives a schematic diagram of the circumstellar environment of α Ori over a distance of 40 stellar radii, together with the inferred temperatures in the different regions.

Finally, our modeling of the chromospheric dynamics also raises the question of what can provide sufficient momentum to drive such oscillations? The upflow and downflow velocities we model range from 5 to -4 km s^{-1}, which compares to the amplitude measured in the optical at Oak Ridge Observatory (Dupree et al. 1999) through a passband of 45 Å centered at 5187 Å (R. Stefanik, 1999, private communication). Optical long-term radial-velocity curves provide amplitudes ranging to $\Delta v \sim 6$ km s^{-1} (see Smith et al. 1989 for an overview). The latter are derived from photospheric metal lines. For comparable mean velocity amplitudes of the photosphere and chromosphere (but not necessarily in phase), by comparing their surface integrated momenta (or the displaced shell mass)—$4\pi R_{\rm ph}^2\, \bar{\rho}_{\rm ph}\, \bar{v}_{\rm ph}\, P$ vs. $4\pi R_{\rm ch}^2\, \bar{\rho}_{\rm ch}\, \bar{v}_{\rm ch}\, P$—one finds that the pulsation of the photosphere can supply far more momentum than is required for chromospheric pulsations of the same amplitude at $R_{\rm ch} \sim 5$–$7\ R_{\rm ph}$. This is because our photospheric densities at $\tau = 1$ are typically of 10^{-9} gr cm^{-3} compared to $\bar{\rho}_{\rm ch} \sim 10^{-16}$ gr cm^{-3}. However, this equation assumes that these densities can be considered as mean values during the oscillation period P. Despite this momentum magnitude difference, by 6 orders of magnitude larger for the photosphere, these low absolute-density values cannot merely be averaged out when considerable time-dependent density changes occur during the pulsations in both atmospheric regions. In other words, density profiles of static atmospheric models are not representative of pulsating supergiant photospheres. The latter requires hydrodynamic modeling, which is outside the scope of our spectral study. Such an integration would first demand the knowledge of detailed evolution in chromospheric upflow and downflow velocities from near-UV emission lines and of its thermodynamic conditions from Hα over at least one pulsation cycle, together with coeval photospheric radial velocity data (i.e., by monitoring unblended atomic lines in the near-IR). Futhermore, this momentum balance must consider the dissipation of piston momentum into highly supersonic small-scale turbulence fields and heating over a

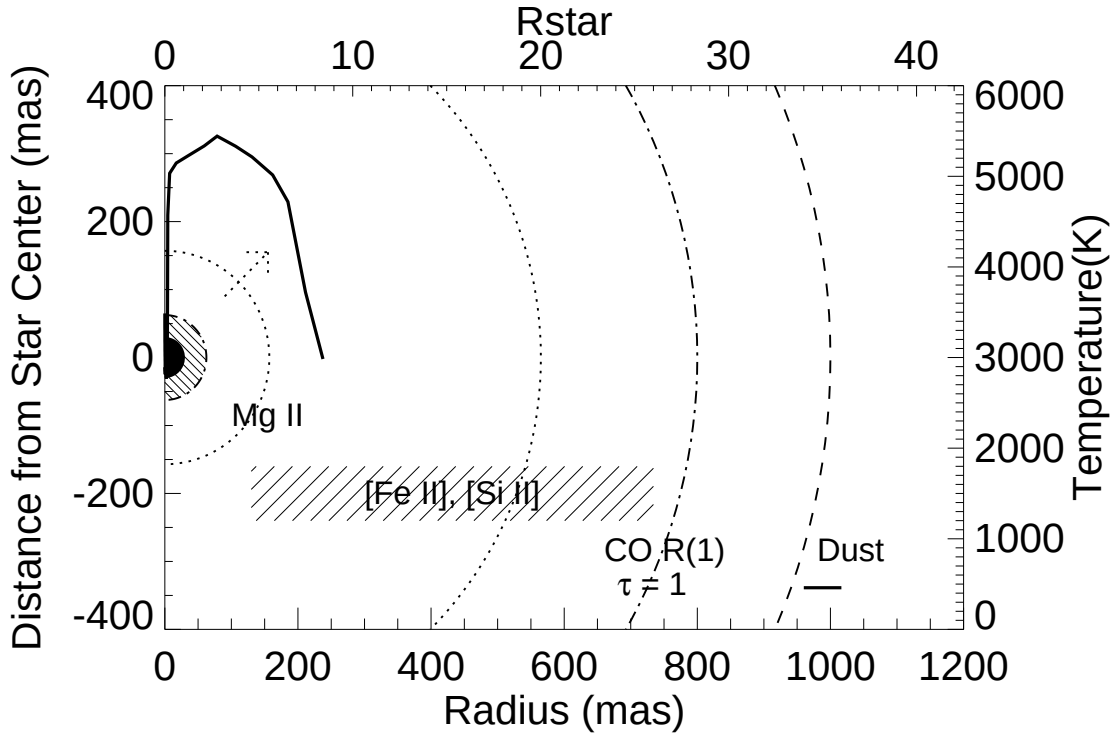

FIG. 10.—Schematic diagram of the various emitting regions in the α Ori atmosphere and their characteristic temperatures (*right axis*). The photospheric radius at 11 μm is shown with solid hemisphere (Bester et al. 1996), the UV continuum radius with hatched hemisphere (Gilliland & Dupree 1996), and the extent of Mg II emission at 2800 Å, which fills the STIS aperture and undoubtedly extends farther (this paper). Radii are drawn to denote the position $20\,R_*$ within which [Fe II] and [Si II] are found (Justtanont et al. 1999), the CO R(1) 4.6 μm line emission radius at $\tau = 1$ in line of sight (Ryde et al. 1999), and the inner radius of the dust shell at ∼1000 mas (Rinehart et al. 1998). Temperature profiles are shown for the chromospheric model in this paper, which extends to $\sim 10\,R_*$, the range of temperatures (1200–1800 K) found from the [Fe II] and [Si II] lines, yielding 1230 K for the excitation temperature of [Fe II] (Justtanont et al. 1999), and the dust grain color temperature of 460 K at 1000 mas (Rinehart et al. 1998). This figure provides a useful guide to the complex atmospheric and circumstellar structure.

very extended atmospheric region that is so typical of Betelgeuse's chromosphere.

7. CONCLUSIONS

1. We have constrained semiempirical models of α Ori's chromosphere based on radiative transfer fits to the Hα line core and the Mg II resonance doublet. The models reveal chromospheric temperatures not exceeding 5500 K and highly supersonic microturbulence velocities ranging to 19 km s^{-1} for a chromospheric extension of $\sim 5000\,R_\odot$ ($\sim 7\,R_*$) above the stellar photosphere. The photospheric microturbulence is ~ 2 km s^{-2}, which strongly increases in the stellar chromosphere.

2. We observe significant intensity variations in the Hα line core between 1993 and 1998. Our modeling indicates long-term changes by ∼400 K in the outer temperature structure of the chromosphere.

3. These temperature changes are clearly correlated with contrast changes observed in optical molecular band heads of TiO. We show that it results from temperature effects by the star's extended chromosphere at the (upper photospheric) formation depths of these bands.

4. From near-UV spectra we measure chromospheric mass movements of 4–8 km s^{-1} between 1998 January and 1999 March. This amplitude corresponds with the amplitude of the photospheric radial velocity curve observed in the optical.

5. We constrain the chromospheric velocity structure from detailed fits to self-absorbed near-UV emission lines. Elaborate modeling of Si I lines shows that this field varies over time. In 1992 there was outflow with a wind accelerating to 4 km s^{-1}, whereas between 1998 and 1999 the mean chromosphere was collapsing onto the photosphere with 5 km s^{-1}. After 1998 April, the inflow decelerated and the scattering cores shift blueward again, indicating recurrent chromospheric upflows.

6. For the phase of strong chromospheric outflow in 1992, we compute a high mass-loss rate of $\sim 5 \times 10^{-7}\,M_\odot$ yr^{-1} but with a subsonic chromospheric terminal velocity of 4 km s^{-1}.

7. The blueshifts after 1998 September are correlated with a significant strengthening in the red emission components of double-peaked lines such as Fe II and Si I. This effect was particularly strong in 1992 when the entire chromosphere was expanding. For example, we measure strong Doppler redshifts by $\sim +0.3$ Å of the red emission maxima in the Mg II resonance doublet.

8. We find that the Mn I resonance line, which blends with the Mg II blue *k* component, is a chromospheric emission transition with a deep and narrow scattering core. In part, this core can contribute to the permanent weakness of the *k* component compared to the strongly variable *h* line and explain the stronger periodicity observed for the latter.

9. We have isolated unblended metal lines in the near-IR for which we measure a macrobroadening and $v \sin i$ of 12 ± 0.5 km s^{-1}, whereas for the Hα core, formed in the upper chromosphere, we measure 18 ± 1 km s^{-1}. This could indicate a rigid rotation of this extended chromosphere or perhaps accelerating large-scale velocity fields in its upper layers for confined regions. On the other hand,

detailed fits to Si I line also reveal a high macrobroadening velocity of 9 ± 1 km s^{-1} in the lower chromosphere, which could point to large-scale turbulence fields extending from the stellar photosphere into the lower chromosphere.

We are indebted to R. Kurucz for help with the LTE spectral synthesis calculations and for many stimulating discussions. R. Gilliland is gratefully acknowledged for assistance with the HST proposal of the STIS observations. We are grateful to I. Ilyin for providing us with high-quality SoFin optical and near-IR spectra. We sincerely thank E. Avrett and H. Uitenbroek for helpful discussions about PRD radiative transfer and for providing us with additional model calculations. The referee, P. Hauschildt, is acknowledged for useful comments. We acknowledge the ING Archive for dearchiving and providing the UES spectra. This research is supported in part by an STScI grant GO-5409.02-93A to the Smithsonian Astrophysical Observatory.

REFERENCES

Allard, F., & Hauschildt, P. H. 1995, ApJ, 445, 433
Anders, E., & Grevesse, N. 1989, Geochim. Cosmochim. Acta, 53, 197
Basri, G. S., Linsky, J. L., & Erikson, K. 1981, ApJ, 251, 162
Beck, H. K. B., Gail, H.-P., Henkel, R., & Sedlmayr, E. 1992, A&A, 265, 626
Bernat, A. P., & Lambert, D. L. 1976, ApJ, 204, 830
Bester, M., Danchi, W. C., Hale, D., Townes, C. H., Degiacomi, C. G., Mékarnia, D., & Geballe, T. R. 1996, ApJ, 463, 336
Boesgaard, A. M. 1979, ApJ, 232, 485
Boesgaard, A. M., & Magnan, C. 1975, ApJ, 198, 369
Bowers, P. F., & Knapp, G. R. 1987, ApJ, 315, 305
Brandt, J. C., et al. 1995, AJ, 109, 2706
Brown, A., Deeney, B. D., Ayres, T. R., Vealé, A., & Bennett, P. D. 1996, ApJS, 107, 263
Carlsson, M. 1986, Uppsala Astron. Obs., Rep. No. 33
Carpenter, K. G. 1984, ApJ, 285, 181
Carpenter, K. G., Pesce, J. E., Stencel, R. E., Brown, A., & Wing, R. F. 1988, ApJS, 68, 345
Carpenter, K. G., & Robinson, D. R. 1997, ApJ, 479, 970
Carpenter, K. G., Robinson, R. D., Wahlgren, G. M., Linsky, J. L., & Brown, A. 1994, ApJ, 428, 329
Carr, J. S., Sellgren, K., & Balachandran, S. 2000, ApJ, 530, 307
di Benedetto, G. P. 1993, A&A, 270, 315
Dulk, G. A. 1985, ARA&A, 23, 169
Dupree, A. K., Baliunas, S. L., Guinan, E. F., Hartmann, L., Nassiopoulos, G. E., & Sonneborn, G. 1987, ApJ, 317, L85
Dupree, A. K., Lobel, A., & Gilliland, R. L. 1999, BAAS, 194, 66.05
Dyck, H. M., Benson, J. A., van Belle, G. T., & Ridgway, S. T. 1996, AJ, 111, 1705
Edmunds, M. 1997, Astron. & Geophys., 38, 27
ESA. 1997, The Hipparcos and Tycho Catalogues (ESA SP-1200)
Fluks, M. A., Plez, B., Thé, P. S., de Winter, D., Westerlund, B. E., & Steenman, H. C. 1994, A&AS, 105, 311
Freytag, B. 2000, in ASP Conf. Proc., Cool Stars, Stellar Systems, and the Sun, 11th Cambridge Workshop, ed. R. J. Garcia Lopez, R. Rebolo, & M. R. Zapatoro Oserio (San Francisco: ASP), in press
Gail, H. P., & Sedlmayr, E. 1998, Faraday Discuss., 109, 303
Gilliland, R. L., & Dupree, A. K. 1996, ApJ, 463, L29
Gray, D. F. 2000, ApJ, 532, 487
Habing, H. J. 1996, A&A Rev., 7, 97
Harper, G. 1994, MNRAS, 268, 894
———. 1996, in ASP Conf. Proc. 109, Cool Stars, Stellar Systems, and the Sun, 9th Cambridge Workshop, ed. R. Pallavicini & A. K. Dupree (San Francisco: ASP), 481
Harrington, J. A., Seel, R. M., Hébert, G R., & Nicholls, R. W. 1970, Identification Atlas of Molecular Spectra (Ontario, Canada: York Univ.)
Hartmann, L., & Avrett, E. H. 1984, ApJ, 284, 238
Hartmann, L., Jordan, C., Brown, A., & Dupree, A. K. 1985, ApJ, 296, 576
Hauschildt, P. H., Allard, F., Alexander, D. R., & Baron, E. 1997, ApJ, 488, 428
Hebden, J. C., Eckart, A., & Hege, E. K. 1987, ApJ, 314, 690
Hubeny, I., & Lites, B. W. 1995, ApJ, 455, 376
Huggins, P. J., Bachiller, R., Cox, P., & Forveille, T. 1994, ApJ, 424, L127
Ilyin, I. 1997, Acquisition, Archiving, and Analysis (3A) Software Package User's Manual (Finland: Univ. of Oulu)
Jacobs, M. L., Porter, D. H., & Woodward, P. R. 1999, BAAS, 195, 110.05
Jennings, D. E., & Sada, P. V. 1998, Science, 279, 844
Justtanont, K., Tielens, A. G. G., M., de Jong, T., Cami, J., Waters, L. B. F. M., & Yamamura, I. 1999, A&A, 345, 605
Knapp, G. R., Phillips, T. G., & Huggins, P. J. 1980, ApJ, 242, L25
Kodaira, K., Tanka, W., Onaka, T., & Watanabe, T. 1979, PASJ, 31, 667
Kondo, Y., Giuli, R. T., Modisette, J. L., & Rydgren, A. E. 1972, ApJ, 176, 153
Kurucz, R. L. 1993, Phys. Scr., T47, 110
———. 1996, in ASP Conf. Proc. 108, Model Atmospheres and Spectrum Synthesis, ed. S. Adelman, F. Kupka, & W. Weiss (San Francisco: ASP), 160
———. 1997, in Proc. First ISO Workshop on Analytical Spectroscopy, ed. A. Heras, K. Leech, N. Trams (ESA SP-419), 193
———. 1998, ASOS6, Abstracts of the Sixth Atomic Spectroscopy and Oscillator Strengths Meeting, Univ. of Victoria, BC, Canada, 89
Lim, J., Carilli, C. L., White, S. M., Beasley, A. J., & Marson, R. G. 1998, Nature, 392, 575
Lobel, A., Israelian, G., de Jager, C., Musaev, F., Parker, J. M., & Mavrogiorgou, A. 1998, A&A, 330, 659
Loup, C., Forveille, T., Omont, A., & Paul, J. F. 1993, A&AS, 99, 291
Monnier, J. D., Geballe, T. R., & Danchi, W. C. 1998, ApJ, 502, 833
Morgan, N. D., Wasatonic, R., & Guinan, E. F. 1997, Inf. Bull. Variable Stars 4499
Morton, D. C. 1975, ApJ, 197, 85
Pasquini, L., Brocato, E., & Pallavicini, R. 1990, A&A, 234, 277
Plez, B. 1998, A&A, 337, 495
Rinehart, S. A., Hayward, T. L., & Houck, J. R. 1998, ApJ, 503, 415
Robinson, R. D., & Carpenter, K. G. 1995, ApJ, 442, 328
Ryde, N., Gustafsson, B., Hinkle, K. H., Eriksson, K., Lambert, D. L., & Olofsson, H. 1999, A&A, 347, L35
Schwenke, D. W. 1998, Faraday Discuss., 109, 321
Schwarzschild, M. 1975, ApJ, 195, 137
Shull, J. M. 1979, ApJ, 233, 182
Singh, P. 1994, MNRAS, 269, 441
Skinner, C. J., Dougherty, S. M., Meixner, M., Bode, M. F., Davis, R. J., Drake, S. A., Arens, J. F., & Jernigan, J. G. 1997, MNRAS, 288, 295
Smith, A. S., Patten, B. M., & Goldberg, L. 1989, AJ, 98, 2233
Trapero, J., Welty, D. E., Hobbs, L. M., Lauroesch, J. T., Morton, D. C., Spitzer, L., & York, D. G. 1996, ApJ, 468, 290
Tsuji, T. 1976, PASJ, 28, 567
Uitenbroek, H., Dupree, A. K., & Gilliland, R. L. 1998, AJ, 116, 2501
van der Hucht, K. A., Haisch, B. M., Stencel, R., & Kondo, Y. 1979, A&AS, 36, 377
Wallace, L., & Hinkle, K. 1996, ApJS, 107, 312
Weymann, R. 1962, ApJ, 136, 844
Wing, R. F. 1992, J. AAVSO, 21, 42
Wirsich, J. 1988, ApJ, 331, 463
Young, J. S., et al. 2000, MNRAS, 315, 635